NORTHWESTERN UNIVERSITY

A MEASUREMENT OF THE RATIO OF PRODUCTION CROSS SECTIONS FOR W+1 JET TO W+0 JETS AT $\sqrt{s}$ =1800 GEV

A DISSERTATION

SUBMITTED TO THE GRADUATE SCHOOL

IN PARTIAL FULFILLMENT OF THE REQUIREMENTS

for the degree

DOCTOR OF PHILOSOPHY

Field of Physics

By

Tacy Marie Joffe-Minor

EVANSTON, ILLINOIS

June 1997

ABSTRACT

A MEASUREMENT OF THE RATIO OF PRODUCTION CROSS SECTIONS FOR $W + 1$ Jet to $W + 0$ Jets AT $\sqrt{s} = 1800$ GEV

Tacy Marie Joffe-Minor

The QCD corrections to W production associated with a jet are studied using the ratio of $W + 1$ Jet to $W + 0$ Jets cross sections for a jet with a transverse energy of 25 GeV. The measured ratio of $0.096 \pm 0.005^{stat} \pm 0.008^{syst}$ is significantly higher than the theoretical predictions of Giele *et al.* of 0.053. This discrepancy is at least partly due to the relatively unconstrained gluon distribution of the proton.

To Ray, with all my love.

Acknowledgements

Life as a physics graduate student is never easy and there are always many people to thank.

First I would like to thank all the women who came before me in this field for making this road a little less treacherous to travel. I hope my presence on the road means that it will. at the very least, feel a little more travels for the women who will come after me.

Next, I want to thank everyone who helped me as a graduate student at Northwestern and at DØ. The first to be thanked are Sharyn Chase and Sean Fleming who were in my classes at NU. We worked and laughed together and kept each other (moderately) sane through two years of classes.

The DØ experiment was already built and taking data when I joined the experiment so, first, I must thank all of the people who designed and built the detector and all of its necessary systems. I also want to thank all of the people who, like me, arrived at DØ after it was built. I want to thank all of them for answering questions, asking questions and being patient while I found the answers. There are a few people who I should specifically thank. Jaehoon Yu's supervision helped me make a great deal of progress in a short time and his continued interest has helped me to understand this analysis better. Frequent conversations with Harry Melanson also assisted the progress of this thesis. Tracy Taylor Thomas's support and

friendship brought a little sanity to what often seemed like a crazy environment. Terry Heuring's visits to my office provided the distraction I needed to work on things with a clear head. My advisor, Heidi Schellman, provided alternating doses of close supervision and loose reins when they were needed making sure I made progress yet allowing me the freedom to make my own mistakes and discoveries.

Next, I want to thank my parents and grandparents for never telling me I could not try something just because I was a "girl". Because of them, when I did finally hear it, I did not believe what I was told. I also want to thank my brother for being my first and longest best friend and for sparking my interest in physics. I really can't thank my entire family enough. They laid the foundations for who I have become.

Last, but not least, I want to thank my husband for all of his support and love. He asked questions about what I was doing and I did my best to answer them and if I was not successful we would try it again. He listened to me rant and rave when things didn't work, and he celebrated with me when they did. He was, and is, a calm voice in a chaotic world and he doesn't always get the appreciation he deserves. Without him I may not have finished. He is, at times, my sanity and always helps me keep my sense of perspective.

Contents

List of Figures

List of Tables

Chapter 1

Introduction

This analysis tests aspects of the theory of strong interactions, Quantum Chromodynamics, or QCD, and utilizes events in which a W boson decayed to an electron and an electron neutrino. The data was collected using the DØ detector at Fermi National Accelerator Laboratory from $\bar{p}p$ collisions during the 1994–1995 run.

1.1 W Production

The production of W's at hadron colliders, specifically, $\bar{p}p$ colliders, is due to the interaction of a quark or gluon from the proton with an antiquark or gluon from the antiproton. The final state consists of the W and, in some cases, additional quarks and gluons. For the purposes of this analysis, only the W's which decay into an electron (positron) and an electron neutrino are used due to the superior electron detection of the detector.

1.1.1 Cross Sections

The proton (and antiproton) are composite particles each consisting of three valence quarks (or antiquarks) and a sea of gluons and quark–antiquark pairs. Since many initial state combinations can produce the same final state configuration the theoretical calculations must sum over all possible combinations. The fractions of the hadrons' momenta carried by the interacting partons vary from event to event and from process to process. For some processes the initial momentum fractions can be deduced from the final state kinematics, for others they cannot. When the momentum fractions cannot be extracted from the data the calculations must integrate over them. The cross section for the production of a W with N jets takes the form

$$\sigma(AB \to W + N) = \sum_{i,j} \int \int dx_1 dx_2 f_i^A(x_1, Q^2) f_j^B(x_2, Q^2) \hat{\sigma}(ij \to W + N) \quad (1.1)$$

where $f_i^A(x_1)$ is the probability for parton i to be in hadron A with momentum fraction x_1 and $\hat{\sigma}(ij \to W+N)$ is the cross section for the production of $W+N$ jets from the interaction of partons i and j. The f's are known as parton distribution functions or PDF's and depend on the momentum fraction, x, of the interacting partons and the momentum transfer, Q^2, in the event. Q^2 is also known as the energy scale of the event. For the theoretical calculations used here $Q^2 = M_W^2$.

The PDF's are produced by collaborations which collect data from experiments that directly probe the constituents of the proton. These collaborations then use fitting methods and DGLAP [1] evolution to generalize the information about the proton to regions of momentum fraction, x, and momentum transfer, Q^2, where

it is not measured. One of the parameters of the fits is Λ_{QCD} which is the energy scale at which the strong coupling becomes large. The strong coupling constant, α_s can be expressed as a function of Λ_{QCD} for one loop as

$$\alpha_s(Q^2) = \frac{12\pi}{(33-2f)\ln(Q^2/\Lambda^2_{QCD})} \tag{1.2}$$

where Q^2 is the energy at which the value of α_s is being evaluated and f is the number of flavors of quarks with masses less than Q^2. Therefore, the PDF's have an internal dependence on α_s. This in turn means that the calculated cross section has a dependence on α_s from the PDF's even if α_s does not appear in $\hat{\sigma}$.

1.1.2 Final States

The simplest way to produce a W at a hadron collider is through the interaction of two quarks, with opposite signs of the third component of their weak isospins, which annihilate with a center of mass energy equal to the mass of the W. In this process only a W is produced. The top Feynman diagram [2] in Figure 1.1 describes this process. Examples of $W^{\pm}$ production are $d + \bar{u} \rightarrow W^-$ and $\bar{d} + u \rightarrow W^+$.

Figure 1.1 also depicts the two possible ways to produce a W in conjunction with a strongly interacting particle, a quark or a gluon, in the final state. The first is just like the production of the W alone except that one of the incoming quarks radiates a gluon before it is annihilated. In the second process the initial particles are a quark and a gluon. The gluon splits into a quark–antiquark pair and one of them interacts with the incoming quark to produce the W. The quark not involved in the creation of the W is then in the final state (lower right diagram

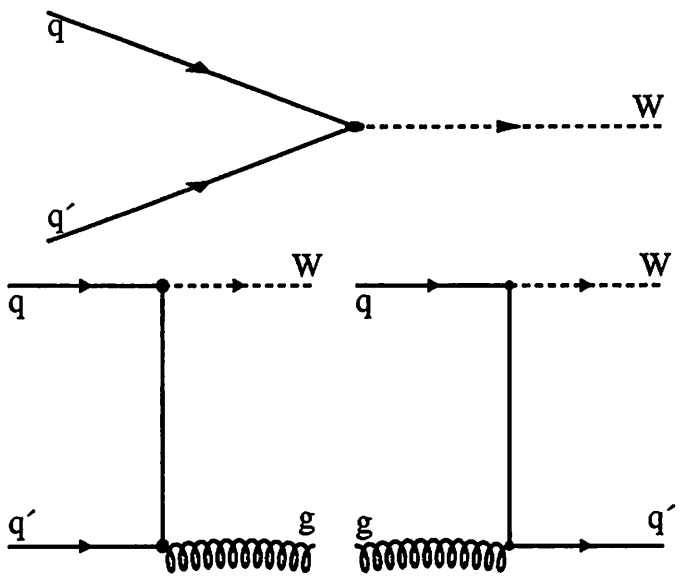

Figure 1.1: Leading order Feynman diagrams for the production of $W + 0$ Jets, top, and $W + 1$ Jet, bottom.

of Figure 1.1). The final state quark or gluon can be identified as a jet. These are the simplest ways to produce $W + 0$ Jets and $W + 1$ Jet. These are the lowest order processes, in terms of α_s, for their production and are referred to as the leading order, LO, processes.

Corrections can be made to the calculations for these processes by going up an order in α_s and including the next-to-leading order, NLO, processes.

For the production of a $W + 0$ Jets, the corrections come in the form of the

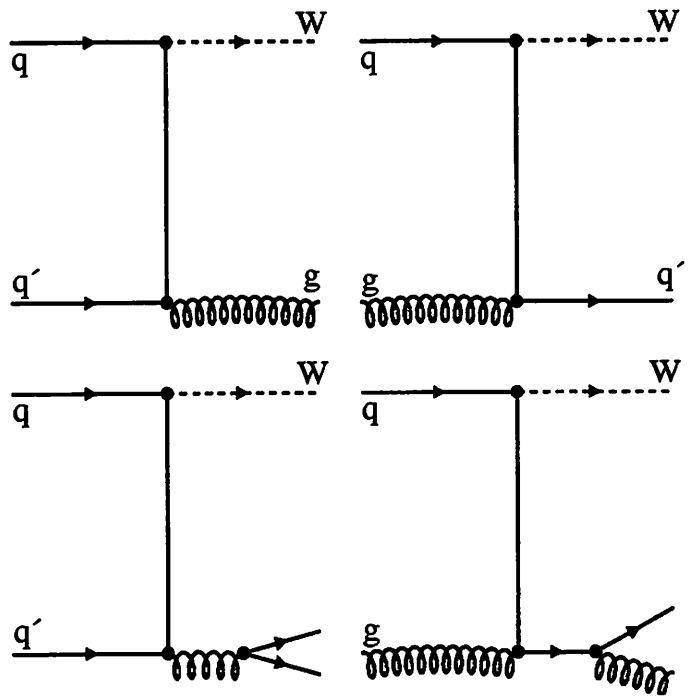

Figure 1.2: Examples of next-to-leading order Feynman diagrams for the corrections to production of $W + 0$ Jets, top, and $W + 1$ Jet, bottom.

production of a W with a jet where the jet does not have enough energy to be found in the detector. For the theoretical calculation, the cut on the transverse energy, E_T, of the parton is a means to prevent infrared divergences in the integration. Another correction for the $W + 0$ Jets is from the interference of the LO process with loop diagrams [2][3]. This part of the correction also cancels some of the infrared divergences in the calculation. The upper diagrams in Figure 1.2 are examples of the diagrams which go into the NLO corrections for $W + 0$ Jets

production.

For $W + 1$ Jet production, the corrections include events from W plus two jets in which one of the jets does not pass the energy cut off. They also include those events in which the two jets are so close together that the they cannot be resolved as separate objects as well as the interference between the LO processes and the loop diagrams.

The NLO corrections bring the theoretical calculations closer to the reality of an experiment using a detector with finite spatial and energy resolutions which cannot measure infinitesimal amounts of energy. They also lessen the dependence of the calculations on the renormalization and factorization scales.

1.2 The Measurement

The measurement in this analysis is the ratio of the production cross sections for $W + 1$ Jet to $W + 0$ Jets in $\bar{p}p$ collisions with a center of mass energy, $\sqrt{s}$, of 1800 GeV. The ratio is expressed as

$$\mathcal{R}^{10} = \frac{\sigma(W + 1Jet)}{\sigma(W + 0Jets)}. \tag{1.3}$$

In the data, a cross section is measured by counting the number of events, N, subtracting contamination, or background, B, from other processes which mimic the process being studied, correcting that number for the acceptance, a, of the detector as well as the efficiency, ε, of the cuts. Finally, the number is divided by

the total luminosity, $\mathcal{L}$, collected,

$$\sigma = \frac{N - B}{\varepsilon \cdot a \cdot \mathcal{L}}. \tag{1.4}$$

The power of a ratio is that some of the factors in the cross section cancel. If all of the factors in the denominator in eq. 1.4 cancel the ratio becomes

$$\mathcal{R}^{10} = \frac{N(W + 1Jet) - B(W + 1Jet)}{N(W + 0Jets) - B(W + 0Jets)}. \tag{1.5}$$

This cancelation minimizes the corrections needed and, therefore, minimizes the sources of error in the measurement. At the very least, the luminosity cancels in the ratio as long as all the events come from the same data set.

1.2.1 What is a Jet

The term jet has different definitions depending on whether one asks a theorist or an experimentalist. A theorist will refer to a final state quark or gluon as a jet while an experimentalist can only see what is left after the parton, a quark or a gluon, has become a colorless particle through fragmentation or hadronization and that particle has interacted with the detector. Only the quark or gluon kinematics are theoretically calculable. Models exist to take these colored partons and turn them into particles but this process is not yet calculable from first principles [4]. On the other hand, a jet for an experimentalists is a large number of particles in a localized area of the detector. These particles are produced when the original colorless object interacted with the detector itself. The experimentalists try to

correct their detector jets for all the changes in the energy of the original particle due to its interaction with the detector to get back to the particle's original energy. This is as close as theory and experiment can get when defining a jet.

1.2.2 $\mathcal{R}^{10}$ versus E_T^{min}

The cross sections for $W + 0$ Jets and $W + 1$ Jet can be written in terms of the strong coupling constant α_s, as

$$\sigma(W + 0Jets) = A_0 + \alpha_s B_0(E_T^{min}) \tag{1.6}$$

$$\sigma(W + 1Jets) = \alpha_s A_1(E_T^{min}) + \alpha_s^2 B_1(E_T^{min}, R) \tag{1.7}$$

where E_T^{min} is the cut off on the transverse energy, E_T, of the jet and R is related to the size of the jet. A_0 and $\alpha_s A_1$ are the LO cross sections for $W + 0$ Jets and $W + 1$ Jet respectively. B_0 is the correction mentioned earlier to the $W + 0$ Jets cross section from $W + 1$ Jet when the jet E_T is too low. It also includes the loop corrections. B_1 depends on E_T^{min} for the same reason B_0 does but it also contains the correction for when two partons are too close together to be resolved as separate entities as well as the loop corrections. The A's and B's in equations 1.6 and 1.7 depend on the PDF's and therefore still depend on α_s even though the α_s dependence of the hard scattering process has been factored out.

Several calculations exist for higher order corrections to W production. A calculation by Arnold and Reno [5] predicts the transverse momentum, p_T, distribution of the W for large p_T's to order α_s^2. Baer and Reno [6] have calculated the order α_s

corrections to W production including interference with loop diagrams. The calculations by Giele, Glover and Kosower [7] calculate $W + 0$ Jets cross sections to order α_S and $W + 1$ Jet cross sections to order α_s^2. These are used in comparisons to the data because they predict the cross sections for exclusive multiplicities. The $W + 0$ Jets to order α_S and $W + 1$ Jet to order α_s^2 calculations are referred to as next-to-leading order calculations throughout this thesis.

Since the W production cross sections depend on the E_T^{min} cut the measured ratio $\mathcal{R}^{10}$ does as well. For that reason, the measurement is made as a function of this cutoff. Because the E_T^{min} cut is only a lower limit on the jet E_T's and no attempt is made to make this a differential measurement as a function of jet E_T, the data points in any plot of a measurement as a function of E_T^{min} are highly correlated as are their errors.

The following chapters describe how the data were gathered, how the events used are selected, what corrections are made to the data and finally the result and conclusions.

Chapter 2

Fermilab and the DØ Detector

The data for this analysis were collected at the Fermi National Accelerator Laboratory, or Fermilab, Tevatron using the DØ detector during the 1994–1995 collider run. The Tevatron is the world's highest energy hadron collider, colliding beams of protons and antiprotons with a center of mass energy, $\sqrt{s}$, of 1800 GeV. The DØ detector is one of two large multipurpose detectors at the Tevatron. It was designed to study many aspects of the products from the proton–antiproton collisions.

2.1 Fermilab and the Tevatron – from Hydrogen to 900 GeV Protons

The Fermilab accelerator complex consists of several different types of particle accelerators, each designed to accelerate the protons (and antiprotons) to a certain energy and then pass them on to the next link in the chain. Figure 2.1 is a schematic of the complex, outlining the various links in the chain. This section outlines how

the beams are created and relies heavily on the information in Ref. [8].

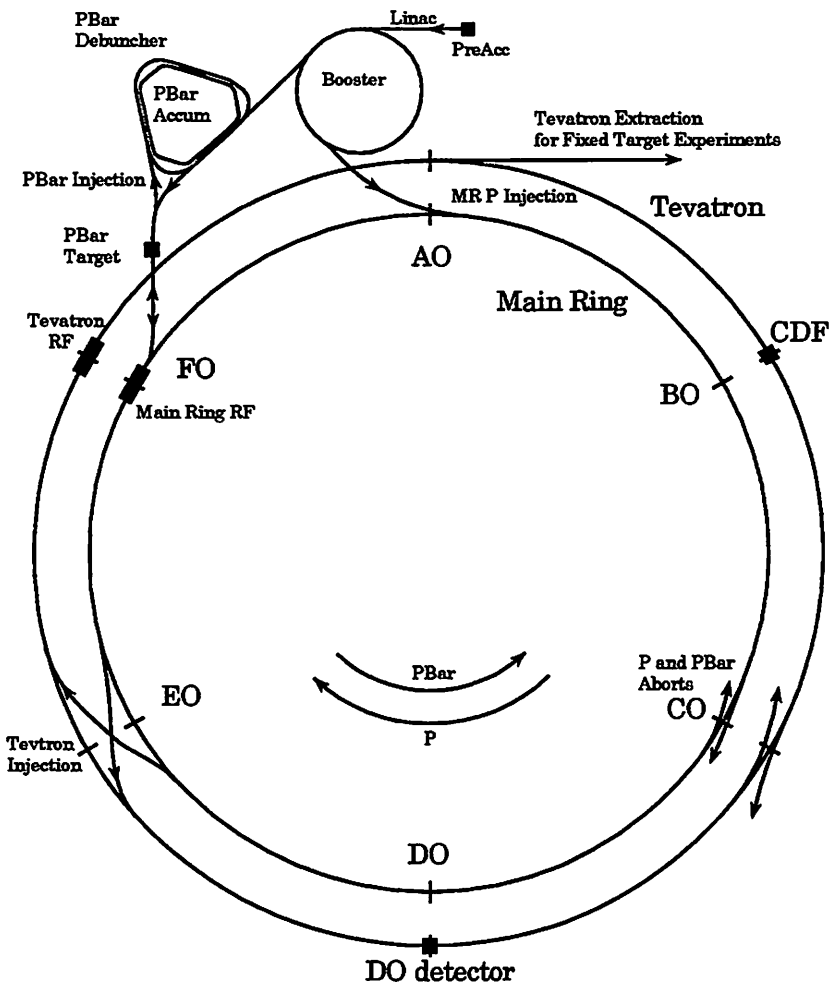

Figure 2.1: Schematic of the Fermi National Accelerator Laboratory

The first step in the process is the production of the bare protons. At the beginning of the process the protons are negatively charged hydrogen ions which are accelerated by a two stage linear accelerator (linac) to an energy of 400 MeV. The electrons are then stripped from the ions and pulsed beams of protons are injected into the Booster.

The charge stripping and the injection into the Booster occur at the same time. This is the stage at which the advantage of starting with H^- atoms is important. The beam of H^- atoms is bent to pass through a stripping foil which removes the electrons. A subsequent magnet then bends the bare protons into the Booster while sending any H^0 and H^- atoms to a beam dump. This makes the transition into the Booster smooth and allows for the elimination of any unstripped atoms from the beam.

The Booster, a fast cycling proton synchrotron, takes the 400 MeV protons from the linac and accelerates them to an energy of 8 GeV in preparation for their injection into the Main Ring.

The Main Ring is a 400 GeV proton synchrotron with a radius of 1000 m. For collider operations at Fermilab, the Main Ring was used as a source of 150 GeV protons to be injected into the Tevatron and as a 120 GeV source of protons to be used in the production of antiprotons.

Antiprotons are produced by colliding 120 GeV protons on a nickel target (other materials have also been used for the target). Approximately 10^5 protons at an energy of 120 GeV are needed to produce just one 8 GeV antiproton. The antiprotons were collected and stored in the $\overline{p}$ accumulator until enough had been collected to inject into the Main Ring so that they too could be accelerated to 150 GeV in preparation for final injection into the Tevatron.

Once the protons and antiprotons in the Main Ring have been accelerated to 150 GeV, they are ready to be injected into the Tevatron. For the data used in this analysis the Tevatron was operating in colliding beam mode. This means that there are actually two beams in the Tevatron circulating in opposite directions at

the same time.

In order to operate in this manner six bunches of protons were injected into the Tevatron from the Main Ring and then six bunches of antiprotons were injected. On average, there were approximately 200×10^9 protons per bunch and 50×10^9 antiprotons per bunch. There were fewer antiprotons in each bunch than protons since the antiprotons are relatively difficult to produce. The longitudinal size of the bunches was about 30 cm while the transverse width and height were approximately 40 μm. Once the twelve bunches were in the Tevatron they were accelerated to the colliding energy of 900 GeV per beam. This created a situation in which the beams crossed approximately every 3.5 μsec. The peak instantaneous luminosity at DØ during the 1994–1995 run exceeded $20 \times 10^{30} \mathrm{cm}^{-2}\mathrm{sec}^{-1}$.

2.2 The DØ Detector

The coordinate system for the DØ detector is such that the positive x-axis is pointing outward along the radius of the accelerator, the y-axis points upward and the z-axis is along the direction of the incoming proton beam. In Figure 2.2 the z axis is oriented along the axis of the central cylinder and the positive x-axis points to the right. Cylindrical coordinates, (r,ϕ,z), are also used such that r is the radial distance from the beam line and $\phi = 0$ is defined to be the positive x-axis. Pseudorapidity is defined in this coordinate system as $\eta = -\ln(\tan(\theta/2))$ where θ is measured relative to the positive z axis (the proton direction) from the interaction point. This definition of pseudorapidity approximates the true rapidity $y = \frac{1}{2} * \ln(\frac{E+p_z}{E-p_z})$, for finite angles, in the limit that the mass is negligible. Rapidity

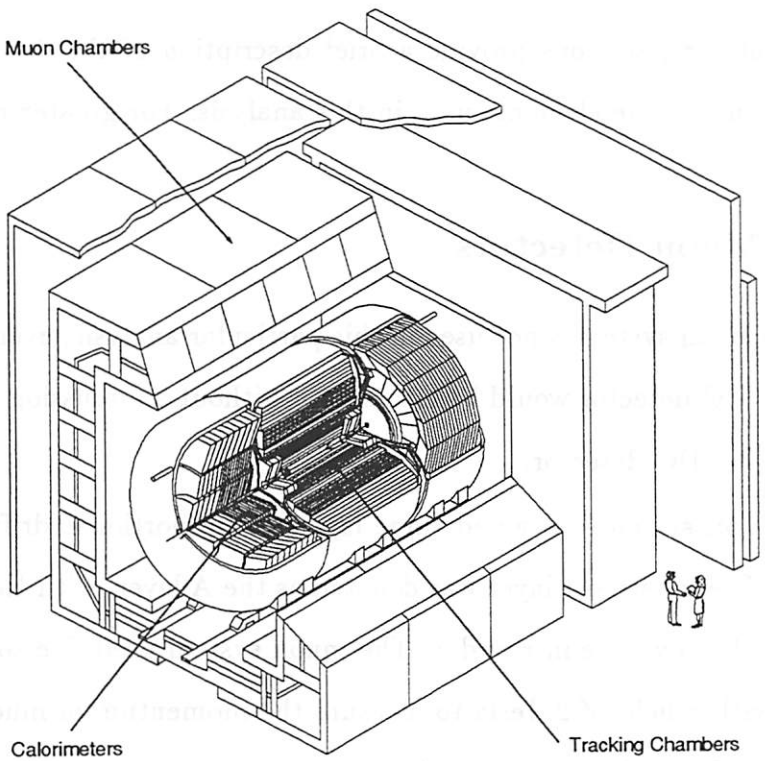

Figure 2.2: A schematic of the DØ detector.

is useful because, although the quantity itself is not a Lorentz invariant, differences in rapidity, Δy, are Lorentz invariant.

The DØ detector consisted of three subsystems centered on the interaction point of the colliding beams and the beam pipe. These subsystems can be thought of as three concentric cylinders with closed ends. The outermost system consisted of muon detectors which covered out to a pseudorapidity of approximately 3.5. The next subsystem was the calorimetry which covered out to a pseudorapidity of 4. The innermost system was comprised of tracking detectors and had a pseudorapidity coverage that approximately matched that of the calorimetry.

The following sections provide a brief description of the detector subsystems concentrating on the elements used in this analysis. For greater detail see Ref.[9].

2.2.1 Muon Detectors

While the muon system is not used in this particular analysis, even a short description of the DØ detector would be incomplete without a discussion of the outermost system of the DØ detector.

The muon system contained three layers of proportional drift tube chambers (PDT's). The innermost layer was denoted as the A layer, with the B and C layers extending the coverage in r and z. The muon system used five solid–iron toroidal magnets with a field of 2 Tesla to measure the momentum of muon tracks. These toroids were located between the A and B layers.

2.2.2 Calorimetry

The middle system of the DØ detector was the calorimetry. Figure 2.3 shows the geometry of the calorimeters and the central tracking. This was the system which measured the energy of all particles produced in the interaction except for muons and neutrinos. The system consisted of three cryostats of sampling calorimeters, arrays of scintillation counters and single readout boards with no absorber plates.

All of the sampling calorimeters used liquid argon (LA) as the active medium. However, different absorber materials were used in various regions of the coverage. The central calorimeter (CC) used depleted uranium, uranium–niobium (2%) al-

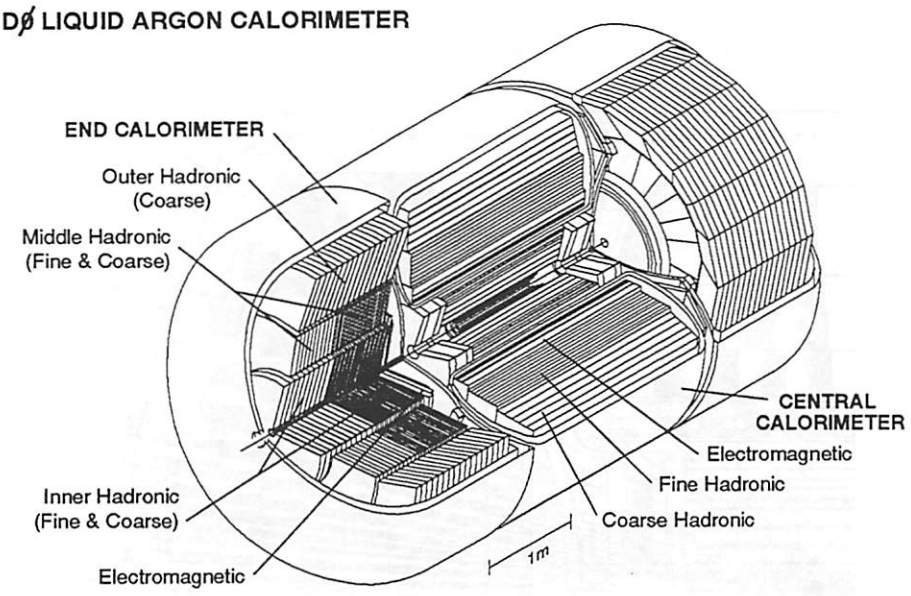

Figure 2.3: An isometric view of the DØ calorimeters and the central tracking.

loy or copper absorbers while the two mirror image end calorimeters (EC's) used depleted uranium or stainless steel as the absorber material.

Central Calorimeter

The central calorimeter is a cylinder centered on the beam pipe and the nominal interaction point. The geometry of the readout of the CC was designed with the interaction point in mind. The cylinder was divided into projective towers which pointed to the nominal interaction point at z=0. The towers had approximate dimensions of 0.1×0.1 in η–ϕ space. The tower structure can be seen in Figure 2.4. The towers were divided into readout cells in concentric cylinders about the beam. The cylinders, or layers, were arranged to provide the best possible measurement of both electromagnetic and hadronic energy depositions. The intersection of the

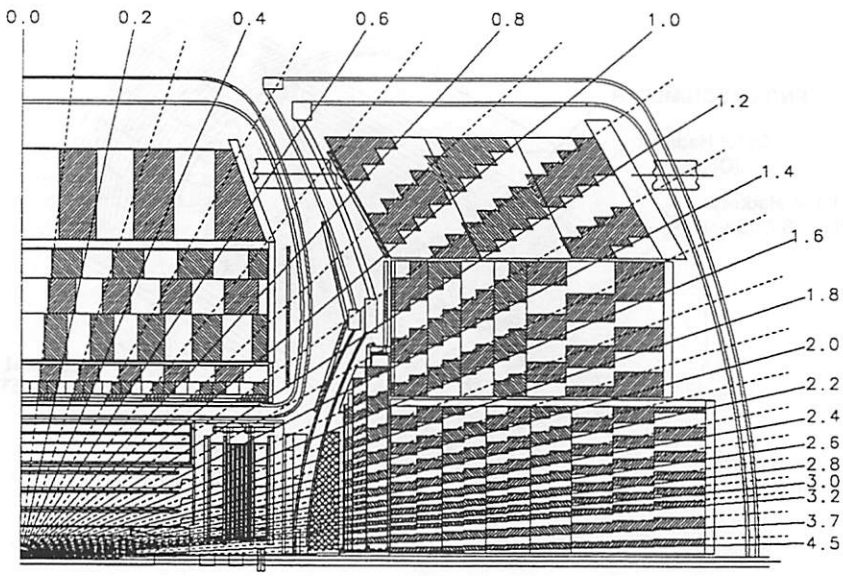

Figure 2.4: Diagram of one quarter of the DØ calorimetry. The calorimeter tower structure is depicted using alternating shaded and non-shaded readout cells.

towers and the layers produced readout units called cells.

The inner layers contained the electromagnetic (EM) modules which used depleted uranium for the absorber plates. Each module actually contained two cells such that there were 32 modules in the ϕ direction. There were 4 readout layers in this section. Layers 1, 2 and 4, in the order of increasing radius, had readout cells of 0.1×0.1 in η–ϕ space. The third layer, which covered the depth of maximum energy deposition for an electromagnetic shower, used finer segmentation of the readout cells resulting in better position measurements of the shower. The segmentation in this layer was 0.05×0.05 in η–ϕ space. The thickness of each of the four layers was 2.0, 2.0, 6.8 and 9.8 radiation lengths, X_0, respectively. The total

interaction length, λ_A, of the central electromagnetic calorimeter was $0.76\lambda_A$. The central electromagnetic layers covered out to a pseudorapidity of $|\eta| \leq 1.2$.

The outer layers of the central calorimeter were the fine hadronic (FH) and the coarse hadronic (CH). The absorber plates for the FH were a uranium-niobium (2%) alloy while the CH plates were copper. There were three separate readout layers for the FH and one for the CH. The coarse hadronic layer captured the end of a hadronic shower while keeping the energy density high in the readout cell and containing the entire shower in the calorimetry. The thicknesses of the FH layers were 1.3, 1.0 and 0.9 interaction lengths, λ_A, while that of the CH layer was 3.2 λ_A. The pseudorapidity coverage for the central hadronic calorimetry was $|\eta| \leq 0.7$ for full coverage and $|\eta| \leq 1.0$ for at least partial coverage.

End Calorimeters

The EC's closed the ends of the cylinder created by the CC. The projective tower structure of the central calorimetry was continued in the end calorimetry. To accomplish this the readout layers were arranged perpendicular to the beam direction and in increasing distance in z from the interaction point as opposed to increasing radius in the CC. The end calorimeters were constructed in three concentric rings creating three distinct modules: inner, middle and outer.

The inner module was the only EC module with electromagnetic calorimetry. The absorber plates for the electromagnetic layers were made of depleted uranium. As in the CC, there were four readout layers but they were arranged in increasing distance in z. The third layer was more finely segmented than the other layers with a segmentation of 0.05×0.05 in η–ϕ space. The thicknesses of the layers

were 0.3, 2.6, 7.9 and 9.3 X_0 in the order of increasing distance in the z-direction, however the cryostat wall in front of the electromagnetic layers increased the total for the first layer to 2.0. The total interaction length for the EC electromagnetic calorimeter was $0.95\lambda_A$.

Beyond the electromagnetic layers (in the z direction) were four layers of fine hadronic cells which used uranium–niobium absorber plates and one layer of coarse hadronic cells which utilized stainless steel absorber plates. Each of the fine hadronic layers had a thickness of 1.1 λ_A, while the coarse hadronic layer had a thickness of 4.1 λ_A.

The middle module formed a ring around the inner module and had a similar layer structure in z. The middle hadronic had four readout layers of fine hadronic each with a thickness of 0.9 λ_A per layer which used uranium–niobium absorber plates. This was followed by one readout layer of coarse hadronic which again employed stainless steel absorber plates with a total thickness of 4.4 λ_A.

The outermost ring in the end calorimetry contained only coarse hadronic cells. The stainless steel absorber plates were inclined 60° with respect to the beam direction toward the center of the detector to retain the projective tower structure used throughout the rest of the calorimeter system.

The electromagnetic coverage for the EC's was $1.5 \leq |\eta| \leq 3.5$. The hadronic coverage was $1.1 \leq |\eta| \leq 4.0$.

There was one major complication to the performance of the DØ calorimetry, the fact that it had an extra accelerator running through it. The Main Ring passed through the coarse hadronic layers at approximately $\phi = \frac{\pi}{2}$ at a radius of about 2 meters from the Tevatron beam pipe. The measures taken to control this

complication will be discussed in Section 2.3.5.

In this analysis the calorimetry is used to measure the total energy and the pattern of the energy deposition for both electromagnetic objects and hadronic jets. In addition, it is used to measure the position of jets and to help measure the position of electromagnetic objects as well as to infer the presence of a neutrino in the event.

Calorimeter Energy Resolutions

The energy resolution of the electromagnetic calorimetry is approximately $15\%/\sqrt{E}$ while the energy resolution of the hadronic calorimetry is approximately $50\%/\sqrt{E}$ [9]. This will be discussed more in Chapter 5.

2.2.3 Inter-Cryostat Region Detectors

The inter-cryostat regions, ICR's, the regions between the central calorimeter and the end calorimeters, contained a great deal of material with little or no instrumentation. Therefore a system of detectors was installed in the regions $0.8 \leq |\eta| \leq 1.4$ to correct for the energy deposited in the uninstrumented cryostat walls and support structures.

The inter-cryostat detector (ICD) consisted of arrays of scintillation counters which were placed between the central calorimeter and the two end cap calorimeters. Single calorimeter readout boards with no absorber plates were also placed inside the end cryostats in front of the middle and outer calorimeter modules as well as at the ends of the fine hadronic in the CC to help instrument this region. The single readout cells are collectively referred to as the massless gaps.

In this analysis, the ICR detectors are used to correct jet energies for the energy deposited in the cryostat walls.

2.2.4 Central Detector

The inner-most system of the DØ detector was the Central Detector and contained all of the charged particle tracking detectors. This consisted of three central subsystems which formed a cylinder centered on the beam and the nominal interaction point and one forward subsystem on either end. The central systems (in increasing radius) were the vertex drift chamber (VTX), the transition radiation detector (TRD) and the central drift chamber (CDC). The forward drift chambers (FDC) closed the tracking cylinder created by the first three subsystems. The relative orientations of these systems is depicted in Figure 2.5.

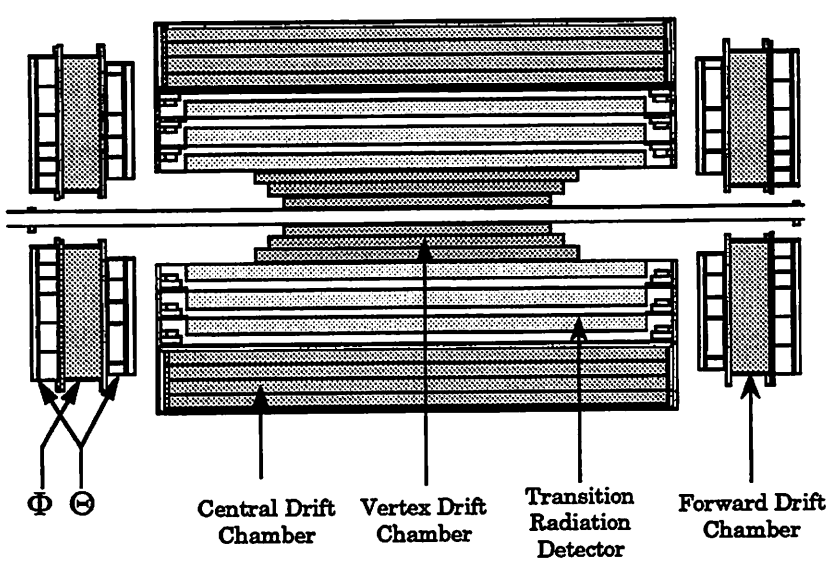

Figure 2.5: The DØ central tracking showing the orientation of the four subsystems.

The signals from all four of the central detectors were digitized in essentially the same manner. They all used a three stage signal processing prescription. The first stage used preamplifiers with a gain of 0.3 mV/fC which were mounted directly on the tracking chambers. The next stage was located outside of the detector volume but still on the detector platform. The signals were transmitted through a system of amplifiers, shaping circuits, and cable drivers. This prepared the signals to be transmitted along 45 m of cable, out of the collision hall to the counting house, for the final stage of the digitization. At this stage the signals were passed through analog buffer amplifier circuits where they were corrected for voltage offsets and gains. They were then digitized in flash ADC's and stored in FIFO circuits. The signals were zero suppressed at this stage to prevent the signals from overloading the data aquisition system.

VTX

The VTX was the innermost detector of the the entire DØ system. It consisted of three concentric layers of drift chambers which measured the r-ϕ coordinates of charged tracks passing through the detector. The VTX covered a pseudorapidity range of $|\eta| < 2$ and measured the trajectory of charged particles passing through it.

TRD

The Transition Radiation Detector (TRD) consisted of three concentric units with radiator and X-ray detection in each layer. The coverage of this system extended to a pseudorapidity of 1.3 ($|\eta| < 1.3$). The TRD could be used to separate electrons

from pions but is not used in this analysis.

CDC

The Central Drift Chambers, or CDC, surrounded the TRD and consisted of four concentric rings of 32 azimuthal cells which were used to measure the trajectory of charged particles passing through them. Each cell contained 30 sense wires which were read out at one end and measured the r-ϕ position of the hits. Each cell also contained two delay lines which were read out at both ends and provided a measurement of the z-position of the hits.

FDC

The Forward Drift Chambers, or FDC's, closed the ends of the tracking cylinder produced by the previous three systems and measured the trajectory of charged particles passing through it. The FDC's covered a pseudorapidity range from ± 1.5 to ± 3.0. Each end had three sets of detectors, a Φ module and two Θ modules (see Figure 2.6). The Φ module had radial wires and, as the name indicates, these measured the ϕ coordinate of the charged tracks passing through it. The Θ modules sandwiched the Φ module and were rotated 45° in ϕ relative to each other. They each consisted of four quadrants with six rectangular cells at increasing radii. Each Θ cell contained eight sense wires and one delay line and measured the θ coordinate of the charged track.

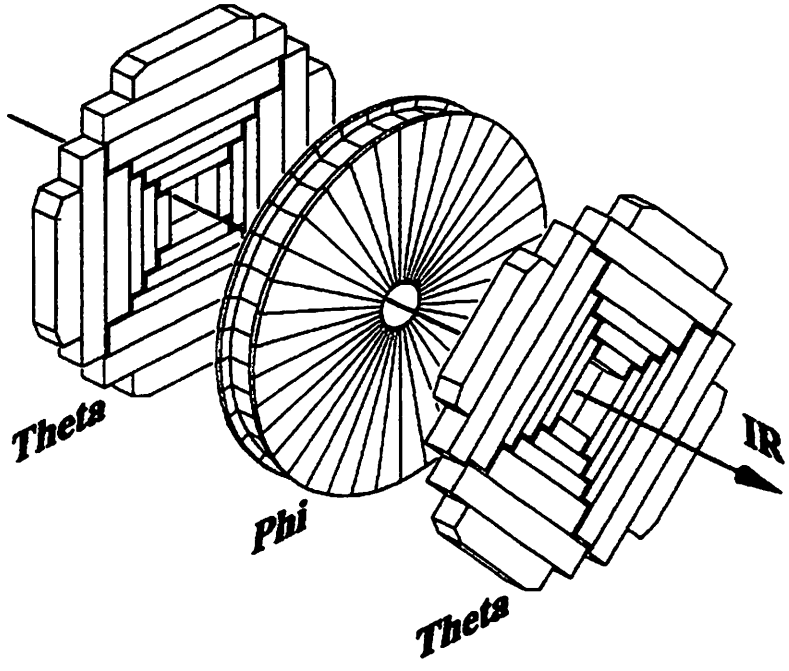

Figure 2.6: An exploded view of one set of detectors in the FDC.

Tracking Uses

The charged tracks in the VTX, CDC and FDC are used to determine the z-position of the event vertex for each event. In addition, an electromagnetic cluster in the calorimeter must have a track pointing to it from either the CDC or the FDC to be considered an electron candidate. This will be described in more detail in Chapter 3.

Tracking Resolutions and Efficiencies

Tracking efficiencies are defined for the efficiency for a tracker to separate two charged tracks at a specific separation. The VTX was 90% efficient for separating r-ϕ track separated by 0.63 mm. The track resolution for the VTX was 50 μm.

The CDC and the FDC were 90% efficient for r-ϕ separations of 2 mm and had resolutions between 150 and 200 μm. The resolution for the z measurement of tracks in the CDC was 2 mm and in the FCD was 4 mm.

2.3 Triggering and Data Aquisition

When an interaction occured in the detector a decision had to be made whether or not the event was interesting before it was saved. This was due to the fact that the rate of interactions in the $\overline{p}p$ crossings was orders of magnitude higher than the rate that events could be written to tape. The reduction in rate was made in several steps.

The raw interaction rate was 150 kHz for a luminosity of 5×10^{30}. The maximum rate would be that given by the beam crossing time, 280 kHz. The Level Ø trigger reduced this rate slightly and indicated whether or not an inelastic collision between a proton and an antiproton had occurred. This rate was reduced by the Level 1 triggers to at most 200 Hz. This was in turn reduced by the Level 1.5 trigger to approximately 150 Hz. The Level 2 trigger filters reduced the rate to 2-3 Hz. The ultimate limiting factor was 3 Hz out of Level 2 since that is the fastest the data could be written from disk to storage tapes. Each of these triggering levels is described in more detail below.

Each level of the trigger made more sophisticated decisions based on more information. Because of this, each level took longer to make the decision and therefore the rejection of the previous levels had to reduce the rate enough that the dead time, the time in which the detector can not be read out because the

data can not be passed to the next level, is minimized. The dead time was held to a maximum of 5-10% by adjusting prescales. A prescale of N means that the system counts how many events pass a specific trigger or filter but only every N^{th} event which passes is retained. The rest of the events are discarded. Prescales were available at both Level 1 and Level 2.

The first three levels of triggering at DØ are hardware triggers. The logic simply rejected or accepted events based on the number of hits in a system or the amount of energy deposited in the calorimeter. The fourth level (Level 2) was a software trigger where actual objects could be partially reconstructed and rejection decisions were based on the reconstructed quantities.

2.3.1 Level Ø

The Level Ø detector was an array of scintillation counters placed close to the beam pipe at either end of the detector between the EC's and the FDC's. These served two purposes.

The first purpose of the Level Ø was to signal when an inelastic collision had occurred. This was done by simply requiring that there be a minimum number of hits in the scintillation array at both ends of the detector. This indicated that both the proton and the antiproton had broken up in the collision.

The Level Ø detectors were also used to monitor the luminosity of the beams. This was done by measuring the rate of non-diffractive inelastic collisions.

In the 1994-1995 run it was not necessary for the Level Ø to indicate an inelastic collision had occurred in order to read out an event. Some triggers made no Level Ø requirement while others actually required very few or no hits in one or both

sides of the Level Ø detector.

2.3.2 Level 1

The Level 1 triggers used no tracking information in the decision making process. They could use information from the calorimeters and the muon system. For this analysis only calorimeter based triggers are used.

The calorimeter triggers required that a certain amount of energy be detected in a specified number of trigger towers. A trigger tower consisted of four calorimeter towers ganged together to form a fast readout unit with the dimensions of 0.2×0.2 in η–ϕ space. There were two types of trigger tower. A jet trigger tower included both the electromagnetic and hadronic, excluding the CH, layers of the towers while an EM trigger tower only included the electromagnetic layers in the tower. Only electromagnetic trigger towers are used to take the data for this analysis.

2.3.3 Level 1.5

The Level 1.5 trigger was first implemented for muon detection and later the ability to refine electron and photon triggers was added. For these triggers it was possible to tighten the transverse energy, E_T, cut on the electromagnetic object as well as place a preliminary cut on the fraction of energy in the object that was measured in the electromagnetic calorimetry. For more information on the Level 1.5 trigger see Ref. [10].

The Level 1.5 electromagnetic algorithm used the E_T of an electromagnetic trigger tower that fired Level 1 plus the E_T in the highest E_T electromagnetic

trigger tower next to it in either the η or ϕ direction. Diagonal neighbors were not used. An E_T cut could then be placed on the cluster. The electromagnet fraction was also calculated by dividing the E_T in the electromagnetic part of the towers by the E_T in the full trigger towers (hadronic plus electromagnetic).

2.3.4 Level 2

The Level 2 trigger filters were software triggers which utilized a farm of 48 parallel nodes connected to the readout of all detector components. At this level, fast reconstruction algorithms were used to cluster calorimeter towers into cone jets and electromagnetic candidates and a fast tracking algorithm created tracks from hits in the central tracking detectors and then loose matches could be made between tracks and electromagnetic candidates. The shape of electromagnetic showers were also checked to match the shape of known electromagnetic showers from test beam data.

There were three parts to most electromagnetic filters. The first was an E_T cut on the cluster, L2ET. The second was a cut on how well the energy profile of the cluster matched the shower shapes of electrons in the test beam, L2ELE. The third term was a cut to ensure that the electromagnetic object was isolated from other objects in the event, L2ISO.

Other Level 2 filters reconstructed muon tracks or required certain amounts of missing transverse energy, $\not\!\!E_T$, in the calorimeter. The missing transverse energy was calculated by requiring that the vector sum of the transverse energy in the calorimeters balance. The amount of imbalance is the $\not\!\!E_T$.

2.3.5 The Main Ring Veto

Because the Main Ring passed through the DØ calorimeter, when there was beam in the Main Ring it could cause energy to be deposited in the DØ detector. There were two timing windows when this was most extreme. One was known as MRBS_LOSS and this occurred early in the Main Ring acceleration cycle when losses in the Main Ring were high. The other window was known as MICRO_BLANK. This occurred when there was beam in the section of the Main Ring that was in the DØ detector. The Main Ring Veto [11] system allowed events to be rejected when either of these conditions occurred, however, not all triggers required this veto. Flags were also set in the data so that any events taken when these conditions did occur could be studied and/or rejected at the offline analysis stage.

2.3.6 The Data Aquisition System

The data aquisition system (DAQ) monitored all of the above systems and more. It monitored the trigger rates, high voltage levels, conditions of the gases used in the tracking chambers and warned the user when these were out of tolerance or not working at all. The DAQ also facilitated the transfer of events which had passed Level 2 filters from the Level 2 nodes onto storage disks and then on to 8 mm storage tapes.

Chapter 3

Particle Reconstruction and Identification

For this analysis several objects must be identified in each event. The decay products of the W boson are used to select the events. Only the events in which the W decayed to an electron and an electron neutrino, $W \rightarrow e\nu$, are used. In order to categorize the events by jet multiplicity, the number of hadronic jets in the event must be known, therefore, the jets must also be identified.

The particle identification begins with the offline reconstruction software, usually referred to as DØRECO. The raw data is read off of the tapes written by the DAQ into a computer farm where a sophisticated form of the Level 2 code, DØRECO, can analyze it. Since there is no dead time constraint for the offline reconstruction, time can be taken to carefully analyze the shower shapes in the calorimeter, combine hits in the tracking detectors to form tracks, and to match the tracks to the showers. The tracks can also be used to determine the z-position

of the event vertex, the point where the hard collision of the proton and the antiproton occurred.

3.1 The Event Vertex

The z-position of the event vertex is one of the first quantities to be reconstructed in each event. This is necessary since many other quantities are later calculated with respect to the position of the vertex. The vertexing algorithm can reconstruct more than one vertex.

The first step in defining an event vertex is to reconstruct all of the charged particle tracks in the three tracking system; VTX, CDC and FDC. These tracks are then extrapolated to the beam position (x=0,y=0) and the z position where the track would intersect the beam is calculated. This is done for all tracks, and the z positions of the intersections are stored so that they can be clustered. A Gaussian fit is made to each cluster of z positions and the position of the vertex is the mean of the Gaussian.

The primary vertex is defined as the vertex with the most tracks used to define it. If the algorithm can not find a vertex the event vertex position is set at z=0 and all subsequent quantities are calculated relative to the center of the detector.

The vertex position can be biased by the number of tracks in the event. Events with larger track multiplicities can have wide distributions of track intercepts with the mean shifted from the true vertex position. This is due in part to the fact that the vertex determination did not weight the tracks which point toward large amounts of energy in the calorimeters. In extreme cases of this, two vertices are

reconstructed and the primary vertex is defined to be the one with the most tracks although the track which points to a large energy deposition in the calorimeter does not point to that vertex. This becomes important when the electron efficiencies are discussed in Section 5.1.2.

3.2 Electrons

Two types of electromagnetic objects were formed in the DØRECO code, PELC's and PPHO's. A PELC is an electron candidate consisting of a cluster of energy in the electromagnetic calorimeter and a track pointing from the cluster to the primary vertex. A PPHO is a photon candidate which is an electromagnetic cluster with no track pointing to the primary vertex.

Electromagnetic objects are formed in the calorimetry using a nearest neighbor clustering algorithm. The first step is to make a list, in the order of descending E_T of all of the EM towers above a 50 MeV threshold. In this case, an EM tower consists of the four EM layers and the first layer of the fine hadronic (FH) calorimeter. Next, the highest E_T tower is taken as the seed for the first cluster. The next step is to sum the E_T of all towers adjacent to the seed tower that have an E_T greater than 50 MeV. Then all towers adjacent to the previous towers, with an E_T greater than 50 MeV, are added to the sum. This continues until there are no towers adjacent to the cluster which have an E_T greater than 50 MeV. Now, the next highest E_T tower that is not already in a cluster is chosen as the next seed and the clustering process is repeated around it. This is continued until all towers above threshold are included in a cluster.

A cluster is kept as a candidate if it has an E_T greater than 1.5 GeV, the highest E_T tower in the cluster has at least 40% of the total E_T of the cluster and if the electromagnetic fraction of the cluster is greater than 90%. The electromagnetic fraction, EMf, is defined as

$$EMf = \frac{E_{EM1} + E_{EM2} + E_{EM3} + E_{EM4}}{E_{EM1} + E_{EM2} + E_{EM3} + E_{EM4} + E_{FH1}}. \tag{3.1}$$

The distinction between a PELC and a PPHO is made by using the tracking. If the EM cluster has a track which points from the cluster to the primary vertex in a road of 0.1×0.1 in θ-ϕ space around the center of the cluster, the cluster is classified as a PELC. If there is no track which points from the cluster toward the primary vertex in the road, the candidate is classified as a PPHO.

Once a PELC or PPHO is identified in DØRECO, the software then computes variables based on the transverse and longitudinal shower shape which can be used later to determine the quality of a given candidate.

From test beam data of a section of the DØ calorimeter and from Monte Carlo simulations of the calorimeter response to electrons and pions a 41x41 covariance matrix was formed to help identify electrons. The matrix took the form

$$\mathcal{M}_{ij} = \frac{1}{N}\sum_{n=1}^{N}(x_i^n - \langle x_i \rangle)(x_j^n - \langle x_j \rangle). \tag{3.2}$$

where x_i^n is the value of observable i for electron n and $\langle x_i \rangle$ is the mean value of observable i for the sample of N electrons used to form the matrix. Some of the observables used include the fraction of the shower energy in layers 1, 2 and 4 of the electromagnetic calorimeter, the logarithm of the shower energy, and the

position of the event vertex along the beam. The inverse of the matrix, $\mathcal{H} = \mathcal{M}^{-1}$ is used in the calculation of a likelyhood parameter, χ^2, for a candidate electron

$$\chi^2 = \sum_{i,j}(x_i^k - \langle x_i \rangle)\mathcal{H}^{ij}(x_j^k - \langle x_j \rangle). \tag{3.3}$$

The χ^2 variable can then be used to eliminate most pions from a sample of candidate electrons. For more information about this quantity and the observables used to derive it, see Reference [12]. The specific cut used in this thesis will be discussed later.

The electromagnetic shower must also be well isolated from other objects in the calorimeter, whether they are other electrons, photons or hadronic jets. The isolation is quantified by comparing the energy in the center of the shower to that in the rest of the shower. For this analysis it is quantified as a fraction, f_{iso},

$$f_{iso} = \frac{E^{total}_{\Delta R=0.4} - E^{EM}_{\Delta R=0.2}}{E^{EM}_{\Delta R=0.2}}, \tag{3.4}$$

where ΔR indicates the radius of a cone, in η-ϕ space, around the center of the shower.

As was discussed previously, an electron in the detector must also have a track which points to the electromagnetic cluster in the calorimeter. This is usually a track in the CDC or the FDC but it can also be a track in the VTX. The degree to which the track and the cluster match is quantified and called the track match

significance. The variable used is σ_{track} and is defined as

$$\sigma_{track} = \sqrt{(\frac{R\Delta\phi}{R\delta\phi})^2 + (\frac{\Delta z}{\delta z})^2} \tag{3.5}$$

for central electrons, where R is the radial distance from the event vertex to the cluster,

$$\Delta\phi = \phi_{track} - \phi_{cluster}, \tag{3.6}$$

$$\Delta z = z_{track} - z_{cluster} \tag{3.7}$$

and $R\delta\phi$ and δz are the position resolutions of the calorimeter in the azimuthal and beam directions, respectively. For this calculation $R\delta\phi = 0.26$ cm and $\delta z = 2.1$ cm. In this case R is the radial distance to the third electromagnetic layer.

For electrons in the EC's the formula takes the form

$$\sigma_{track} = \sqrt{(\frac{\Delta r}{\delta r})^2 + (\frac{r\Delta\phi}{r\delta\phi})^2} \tag{3.8}$$

where δr is the radial resolution in the EC and $r\delta\phi$ is the azimuthal resolution.For the EC calculation $\delta r = 2.0$ cm and $r\delta\phi = 0.5$ cm. In this case, r is the radial distance from the beam to the position of the shower in the third electromagnetic layer.

3.3 Neutrinos

The most difficult particle to measure is the one which rarely interacts with anything. Neutrinos are examples of such particles. Their presence can be inferred

from other information in the event. Because the actual collision is between a parton from the proton and a parton from the antiproton the z component of the momentum of the two colliding particles is not known. However, since the x and y components of the momentum of the colliding particles are assumed to be negligible, conservation of energy and momentum can be used to determine the imbalance in E_T or the transverse part of the missing energy, $\not\!\!E_T$. A large amount of $\not\!\!E_T$ in an event is used to indicate the presence of a neutrino in an event.

DØRECO actually calculates the $\not\!\!E_T$ three times. The first calculation is based only on the vector sum of the transverse energy in the calorimeter towers. The $\not\!\!E_T$ is the amount of transverse energy needed to make the vector sum equal zero. The second calculation corrects the first for the energy measured in the ICR detectors. The third then corrects this for the energy of any muons detected in the event. This analysis uses the second calculation corrected for various calibration corrections which will be described in Chapter 5.

3.4 Jets

Hadronic showers are reconstructed using two different algorithms. One is the nearest neighbor algorithm similar to the one used for electrons described in Section 3.2. The other is an iterative fixed cone algorithm which also starts with seed towers but then combines the towers if they are within a radius R in η-ϕ space of the seed tower. Before anything is done in the identification of seed towers or in the clustering, the E_T, η, and ϕ of each tower are recalculated with respect to the primary vertex as opposed to the center of the detector.

The cone algorithm starts by first making a list of seed towers arranged in descending values of E_T. A tower is put into the list if its E_T is greater than 1 GeV. Preclusters are then formed. Precluster formation uses the (η,ϕ) position of the seed tower as the center of a cone with radius $R = 0.3$ ($R = \sqrt{\Delta\eta^2 + \Delta\phi^2}$). All towers with an E_T greater than 1 GeV within the cone are summed and the E_T weighted center in η-ϕ space is calculated and stored. All towers in the precluster are removed from the seed list and the next highest remaining seed tower is used to form the next precluster. This is continued until all seed towers are included in a precluster. The preclustering is performed to reduce the number of seeds the next step in the jet clustering algorithm must consider.

Jet clustering begins by ordering the preclusters in descending E_T. The η-ϕ position of the highest E_T precluster is used as the center of a cone of radius R and all towers within that cone are summed. The E_T weighted centroid is calculated using

$$E_T^{jet} = \sum_i E_T^i \tag{3.9}$$

$$\eta^{jet} = \frac{\sum_i E_T^i \times \eta_i}{\sum_i E_T^i} \tag{3.10}$$

$$\phi^{jet} = \frac{\sum_i E_T^i \times \phi_i}{\sum_i E_T^i} \tag{3.11}$$

where $\sum_i$ is a sum over all towers in the cone. If the η-ϕ position of the centroid of the jet is not within $R = 0.001$ of the previous center, the new η-ϕ position is used as the center for a new cone and the process is repeated until the distance is less than 0.001 between the new and the old centers. To prevent the algorithm from oscillating between two positions indefinitely, a cutoff of 50 iterations is imposed.

Once a stable jet is achieved the position of the jet is recalculated using a different definition for the angles.

$$\phi = \tan^{-1}(\frac{\sum_i E_x^i}{\sum_i E_y^i}) \tag{3.12}$$

$$\theta = \tan^{-1} \frac{\sqrt{\sum_i E_x^{i2} + \sum_i E_y^{i2}}}{\sum_i E_z^i} \tag{3.13}$$

$$\eta = -\ln(\tan \frac{\theta}{2}) \tag{3.14}$$

where, again, the $\sum_i$ is over all towers in the jet and E_x^i, E_y^i and E_z^i are the three components of the energy vector of each cell. If the E_T of the jet is less than 8 GeV the candidate is not saved.

The next jet starts with the next highest precluster that is not within $R = 0.35$ of the center of a previously found jet, and the clustering follows the same iterative method.

This continues until all preclusters have been included in a jet. The entire process is repeated for several different jet cone sizes but using the same preclusters. At DØ the cone sizes used for jets are 0.3, 0.5, 0.7 and 1.0.

There are a few quantities used to eliminate jets which are created due to detector effects or those which are not produced by a quark or gluon but are actually misidentified particles. These quantities are based on ratios of jet energies deposited in different parts of the calorimeter.

The coarse hadronic fraction, CHf, is the ratio of the energy in a jet deposited

in the coarse hadronic layers of the calorimetry to the total energy of the jet,

$$CHf = \frac{E^{CH}}{E^{tot}}. \tag{3.15}$$

A cut on this can eliminate jets caused by energy deposited in the calorimeter by the Main Ring.

The Hot Cell Fraction (HCf) is the ratio of the highest energy cell in the jet to the second highest energy cell in the jet,

$$HCf = \frac{E^{cell1}}{E^{cell2}}. \tag{3.16}$$

This fraction can be used to remove jets caused by a noisy calorimeter cell.

Finally, the electromagnetic fraction of the jet is the ratio of the amount of energy in the jet deposited in the EM layers of the calorimetry to the total energy in the jet,

$$EMf = \frac{E^{EM}}{E^{tot}}. \tag{3.17}$$

A cut on this quantity removes jets which were actually created by electrons or photons as well as jets caused by noisy electromagnetic cells in the EM calorimeters. The EMf for jets is slightly different than that for electrons since it uses the full hadronic part of the towers instead of just the first layer.

Chapter 4

Data Selection and Background Subtraction

The data selection for this analysis started at the trigger level and continues offline with progressively tighter cuts. The general characteristics of the online data selection were discussed in Section 2.3. The specific requirements will be discussed below.

While the main analysis studies events with a W boson, some efficiency studies are conducted using events with a Z boson. Therefore, the selection of both W and Z events will be described. The types and amounts of background events in the samples will also be discussed along with the methods used to estimate these backgrounds.

4.1 W Boson Events

For this analysis only W events in which the boson decayed to an electron and an electron neutrino, $W \rightarrow e\nu$, are considered. Since DØ did not have a magnetic field in its central tracking volume, electrons and positrons cannot be differentiated and they are both referred to as electrons. The presence of the neutrino in the decay of the W is inferred from a large amount of missing transverse energy, $\not\!\!E_T$, in the event.

Jets are not considered in the selection of W candidates, but they are used in the categorization of the events. Properties of the jets are also used to detect problems in the detector which can affect the quantities used to identify the decay products of the W. For this reason, the jet properties are checked and events with jets created by detector malfunctions or the Main Ring are removed from the sample.

4.1.1 Level Ø and Level 1 Triggers

For part of the 1994–1995 run the first requirement in the trigger sequence was that the Level Ø fired, signaling that an inelastic interaction had occurred. Beginning with run number 85277 this requirement was dropped in the W trigger so that DØ could trigger on diffractively produced W's as well. Later in the analysis, a cut is applied to remove diffractively produced W's from the sample.

At Level 1, the signal trigger required an electromagnetic trigger tower with at least 10 GeV of transverse energy, E_T, in it. For runs prior to run 85277 the threshold was actually 12 GeV. The name of this trigger is EM_1_MAX. Another

trigger, used only in the background studies, had a Level 1 threshold for the electromagnetic object of 7 GeV. The name of this trigger is EM_1_MON.

4.1.2 Level 1.5 Trigger

Beginning with run number 85277, a new tool was added to the electromagnetic triggering, a Level 1.5 electromagnetic tool [10]. The Level 1.5 trigger could check the transverse energy of the electromagnetic object as well as its electromagnetic fraction (Section 2.3.3). For the signal trigger, EM_1_MAX, the E_T cut was 15 GeV. There was no Level 1.5 E_T cut used on EM_1_MON. Starting with run 87804 an electromagnetic fraction cut of 85% was also imposed on the electromagnetic object. The electromagnetic fraction was calculated using the same 2×1 cluster (see Section 2.3.3) used to calculate the E_T and was the ratio of the electromagnetic E_T to the total E_T in the towers. This level of triggering was added to both of the Level 1 triggers discussed in the previous subsection. This provides some rejection of backgrounds without cutting into the efficiency for real electrons.

4.1.3 Level 2 Filters

The filter for the $W \rightarrow e\nu$ signal used EM_1_MAX for the Level 1 conditions and had several requirements for the electron candidate; it had to have an E_T of at least 20 GeV, it had to pass the shower shape cuts which are based on the shower shapes of test beam electrons, and it had to be isolated from other objects in the calorimeter. In addition the event had to have at least 15 GeV of missing E_T, $\not\!\!E_T$. The trigger filter used for the signal is EM1_EISTRKCC_MS. The name of this

trigger implies that if the cluster was in the CC it had to have a track pointing to it to pass the trigger. Due to a flaw in the logic used to define the trigger, however, this was never enforced. The integrated luminosity for the signal trigger is approximately 83 pb^{-1}.

There are also several Level 2 trigger filters used for $W \rightarrow e\nu$ background studies. Two of these had an E_T cut of 20 GeV and a shower shape cut but no isolation cut on the electron candidate, EM1_ELETRK_MON and EM1_ELE_MON. The EM1_ELETRK_MON filter also had a requirement that the electromagnetic cluster have a track pointing to it while the other filter did not. These filters used the same Level 1 and Level 1.5 conditions as the signal filter. After run number 85277 EM1_ELETRK_MON did not exist.

In addition, there are two other trigger filters, ELETRK_1_MON and ELE_1_MON, which only differ by a tracking requirement which are also useful for W background studies. They require that there be an electron candidate in the event with an E_T of at least 16 GeV which passes the shower shape cuts. Again there is no cut on the isolation of the object. The ELETRK_1_MON filter required a track to match the electromagnetic cluster. These filters used the EM_1_MON trigger for their Level 1 conditions which had a lower E_T requirement than the signal trigger.

4.1.4 Offline Cuts

Once the data has been written to tape and reconstructed, more cuts can be applied to refine the sample. These cuts can be grouped in several categories: event cuts, electron cuts, jet cuts, and a $\not\!\!E_T$ cut.

Event Cuts

The event cuts are designed to eliminate events caused by accelerator conditions or detector effects. Many such events can be eliminated by cutting on trigger conditions and general event characteristics. The event cuts are also used to insure that the objects under study are in good fiducial regions of the detector to guarantee that they are well measured. The event cuts are listed below.

- A cut on beam conditions, eliminating events with conditions MRBS_LOSS and MICRO_BLANK. MRBS_LOSS and MICRO_BLANK are both logicals which indicate the beam conditions in the Main Ring at the time of the trigger. These were discussed in section 2.3.5. This cut eliminates events with large amounts of $\not\!\!E_T$ due to Main Ring activity and reduces the integrated luminosity to 75.9 pb^{-1} for the signal filter. The Main Ring can produce $\not\!\!E_T$ in two ways. One effect is due to the fact that if the Main Ring deposits energy in the calorimeters that is not associated with the hard interaction then the $\not\!\!E_T$ calculation will attempt to balance this, producing a $\not\!\!E_T$ vector pointing away from the Main Ring. The other effect is from energy pileup in the cells around the Main Ring before the $\bar{p}p$ interaction which produces a $\not\!\!E_T$ vector pointing toward the Main Ring.

- A requirement that the LØ counters fired for that event even though the trigger may not have required it. This eliminates any diffractively produced W's from the sample.

- A requirement that the event satisfies either the signal filter or one of the background filters.

- The highest E_T electron candidate must be within the appropriate fiducial volume of the detector ($|\eta^{det}| < 1.0$ and $1.5 < |\eta^{det}| < 2.5$). In this case the detector pseudorapidity, η^{det} is used instead of the pseudorapidity relative to the primary vertex. This ensures that the electron candidate is well measured in the calorimeter.

- The scalar sum of the transverse energy in the event must be greater than 0 GeV and less than 1800 GeV. This cut helps to eliminate multiple interactions and triggers due to noisy calorimeter cells effects.

- All of the jets in the event, if any, must pass the coarse hadronic fraction (CHf) cut, the Hot Cell fraction (HCf) cut and the EM fraction (EMf) cut as described in section 3.4. More details about these cuts, including the cut values, are discussed below.

Electron Cuts

This analysis uses two different sets of cuts for electron candidates. One set is used to identify signal candidates, or objects which are very likely electrons. These will often be referred to as 'good' electrons. The sample defined with these cuts includes signal and background events. The other set of cuts is used to identify a set of electron candidates that are very likely not electrons but are probably highly electromagnetic jets. This set contains predominantly background events and is used in modeling the background from multijet events which will be discussed in section 4.2.1. The electromagnetic objects identified by these cuts are often referred to as 'bad' electrons in this analysis. For an explanation of the cut variables see

section 3.2.

The cuts for a 'good' electron are:

- candidates in the Central Calorimeter must be well away from cracks between calorimeter modules, $0.05 < d\phi_{crack} < 0.95$, where

$$d\phi_{crack} = mod(\frac{\phi^{electron}}{2 * \pi/32}, 1), \tag{4.1}$$

- E_T of the electromagnetic object must be greater than 25 GeV,
- the object must be identified as a PELC by DØRECO,
- the object must pass the Level 2 filter conditions for the signal filter (L2ET greater than 20 GeV, L2ELE and L2ISO),
- the isolation fraction must be less than 0.15, $f_{iso} < 0.15$ (Eq. 3.4),
- $\mathcal{H}$ matrix $\chi^2 < 100$, based on test beam electron shower shapes (Eq. 3.3),
- electromagnetic fraction of the calorimeter shower must be greater than 95%, $EMf > 95\%$, where only the four electromagnetic layers and the first fine hadronic layer are used to calculate the fraction (Eq. 3.1),
- the track match significance must be less than 5, $\sigma_{track} < 5$ (Eq. 3.5) for candidates in the CC and less than 10 for candidates in the EC,
- one and only one electron candidate with an E_T greater than 10 GeV and passing the χ^2, isolation and σ_{track} cuts can be present in the event. This cut is made to eliminate $Z \rightarrow e^+e^-$ events from the sample.

This results in 43299 candidate event from the signal filter in the central calorimeter, CC, and 28931 candidates in the end calorimeters, EC. From the background filters these cuts select 18279 events in the CC and 31624 events in the EC.

The cuts for a 'bad' electron are:

- E_T >25 GeV,
- $\mathcal{H}$ matrix $\chi^2 > 200$,
- $EMf > 90\%$,
- $f_{iso} > 0.15$ or $\sigma_{track} > 10$.

These cuts select 2227 event in the CC and 5887 events in the EC from the signal filter and 8727 event in the CC and 14067 events in the EC from the background filters.

Jet Identification and Cuts

The triggers for this analysis only utilize the electromagnetic object in the calorimeter in their determinations so that any jets in the event are considered to be unbiased. Jets in these event are reconstructed using a fixed cone algorithm with a radius of 0.7 in η–ϕ space.

The jets in the W candidate events must pass quality cuts which eliminate jets created by spurious accelerator or detector conditions. All jets in an event are checked except the jet which corresponds to the electron candidate. The cuts are:

- a requirement that the coarse hadronic fraction is less than 40%, CHf <40% (Eq. 3.15),

- a requirement that the Hot Cell fraction be less than 10, HCf <10 (Eq. 3.16),

- a requirement that the electromagnetic fraction of the jet be less than 95%, EMf < 95% (Eq. 3.17). In this case the full depth of a tower is used to calculate the ratio, unlike the similar fraction for the electrons.

If any jet in an event fails one of these cuts the event is eliminated since jets produced from these effects can bias the measurement of the $\not\!\!E_T$ in the event. This eliminates 6% of the events with a 'good' electron in the CC from the signal filter and 8% of the events with a 'good' electron in the EC. The event statistics listed above reflect this reduction.

In addition to the above cuts on the jets, an E_T cut is used to categorize the event by its jet multiplicity. The E_T of a jet must be greater than a minimum E_T, E_T^{min}, in order to be counted. Any event with a jet which does not satisfy this cut is categorized as having a correspondingly lower jet multiplicity.

Most of the studies use a range of E_T^{min} which extends from 15 GeV to 90 GeV. Some studies eliminate points at one or both ends of this range.

Missing E_T

The signal sample is identified using a cut of 25 GeV on the $\not\!\!E_T$ in the event. Some of the background studies use no $\not\!\!E_T$ cut. The number of good electron events from the signal filter after a 25 GeV $\not\!\!E_T$ cut are 36984 for central electrons and 17954 for forward electrons. Table 4.1 lists the number of events for each multiplicity as a function of E_T^{min} for both electrons in the CC and the EC.

E_T^{min}	CC 0 Jets	EC 0 Jets	CC 1 Jet	EC 1 Jet
15	29007	13811	5952	2711
20	31981	15254	4017	1972
25	33617	16123	2829	1418
30	34599	16685	2067	1021
35	35167	17040	1593	752
40	35532	17270	1290	565
45	35833	17419	1028	452
50	36037	17531	852	354
55	36216	17615	685	283
60	36351	17682	563	225
65	36449	17734	479	183
70	36551	17779	390	141
75	36626	17811	323	114
80	36689	17834	270	95
85	36732	17854	230	78
90	36770	17867	194	67

Table 4.1: Raw candidate event statistics versus E_T^{min} for $W + 0$ Jets and $W + 1$ Jet for both CC and EC electrons.

4.2 Backgrounds in W Events

There are many possible sources of background to $W \rightarrow e\nu$ events. The dominant background for this analysis is produced by multijet events in which one jet fakes an electron by fluctuating highly electromagnetically and the E_T of one or more jets in the event is sufficiently mismeasured that there is also substantial $\not\!\!E_T$ in the event.

Data are used to estimate the amount of this background in the signal sample. Two similar methods are employed to estimate this background. The first is the same as the method used for a previous DØ analysis [13]. The second is an adaptation of that method. Both are described in the following subsections.

Other possible contributors to the background for $W(\rightarrow e\nu)$+ Jets include direct photon events, Drell-Yan and $Z \rightarrow e^+e^-$, $Z \rightarrow \tau\tau$, $W \rightarrow \tau\nu$ and top quark production.

4.2.1 Multijet Background Subtraction

The principle used to estimate the amount of multijet background in the $W \rightarrow e\nu$ sample is quite simple. It is based on the assumption that W decays are the main source of single high E_T electron events at DØ. The neutrino from the W decay is essentially undetectable in the DØ detector and its presence can only be inferred from the substantial $\not\!\!E_T$ in the event. Therefore by selecting events with only one high E_T electron, the sample will have low $\not\!\!E_T$ events which are background and events with larger amounts of $\not\!\!E_T$ which are mostly signal but also include some background events.

The next step is to define a sample of 'bad' electrons. These are actually jets which, at first glance, look like electron candidates but which fail the 'good' electron cuts. The cuts on the electromagnetic object in these samples are designed to select a sample with very few $W \rightarrow e\nu$ events in it. The low $\not\!\!E_T$ events in this sample are produced the same way as the low $\not\!\!E_T$ events from the 'good' electron sample, therefore the $\not\!\!E_T$ distributions can be area normalized to each other at low $\not\!\!E_T$ and the $\not\!\!E_T$ distribution for the 'bad' electrons can then be extrapolated into the signal region, $\not\!\!E_T > 25$ GeV, of the good sample. The assumption is that as the $\not\!\!E_T$ goes to zero the 'good' electron sample is all background.

Method One

The first method for subtracting the background caused by multijet events from $W(\rightarrow e\nu)$+ Jets events only utilizes data from background triggers which do not have a $\not\!\!E_T$ cut in them. Two samples are extracted from the triggers. One sample contains events in which an electron candidate passes all of the cuts used to define the signal sample, 'good' electron. This sample contains both signal and background events. The other sample consists of events in which the electron candidate passed the 'bad' electron cuts. This sample is predominantly background events. The samples are defined for electrons in the Central and End Calorimeters separately for each jet multiplicity and value of E_T^{min}.

The $\not\!\!E_T$ distribution for the 'bad' electron sample is then area normalized to the $\not\!\!E_T$ distribution for the 'good' electron sample in the region of low $\not\!\!E_T$, $\not\!\!E_T <$ 15 GeV. The normalization factor can be expressed as

$$N = \frac{\#\ good\ with\ \not\!\!E_T < 15\ GeV}{\#\ bad\ with\ \not\!\!E_T < 15\ GeV}. \tag{4.2}$$

Figure 4.1 shows this for both the zero jet and the one jet events. The histogram is the $\not\!\!E_T$ distribution for the 'good' electrons and the points are the $\not\!\!E_T$ distribution for the 'bad' electrons after the normalization factor has been applied. The top plots are for events with electrons in the CC with no jets with an E_T greater than 25 GeV. The lower plots are for events with the electron in the CC and one jet in the event with an E_T greater than 25 GeV. The left hand line shows the upper boundary for the normalization region while the right hand line marks the $\not\!\!E_T$ cut used to define the signal region. The vertical scale in the left hand plots is chosen

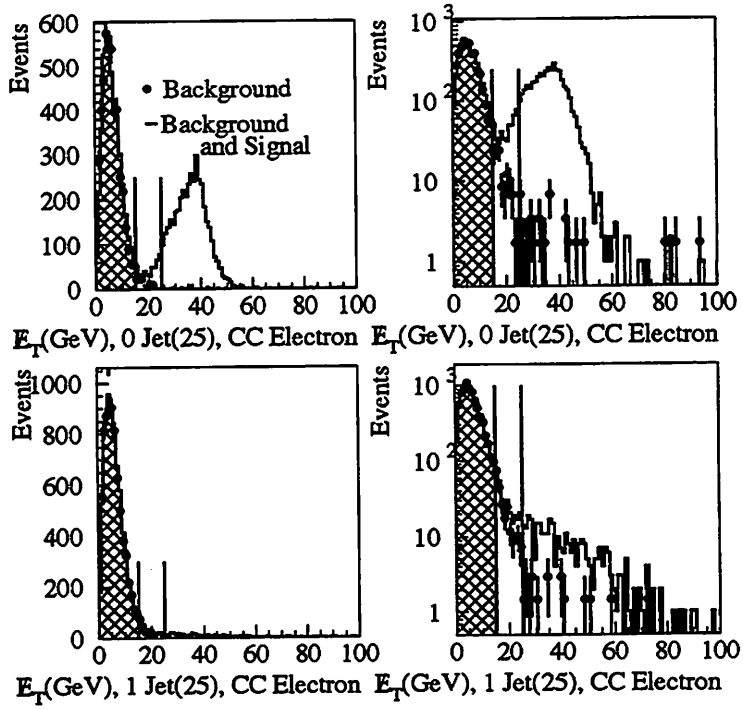

Figure 4.1: Background Subtraction Method 1 – An E_T^{min} of 25 GeV is used here to define the jets. The points are the normalized $\not\!\!E_T$ distribution from 'bad' electrons. The histogram is the $\not\!\!E_T$ distribution for 'good' electrons. The hatched region is the area of normalization.

to highlight the normalization region while the vertical scale in the right hand plots highlights the signal region.

The background fraction in the signal region is simply the number of events from the background sample with $\not\!\!E_T$>25 GeV multiplied by the normalization factor and divided by the number of events with $\not\!\!E_T$>25 GeV from the signal plus background sample

$$B.F. = N * \frac{\#\ bad\ with\ \not\!\!E_T > 25\ GeV}{\#\ good\ with\ \not\!\!E_T > 25\ GeV}. \tag{4.3}$$

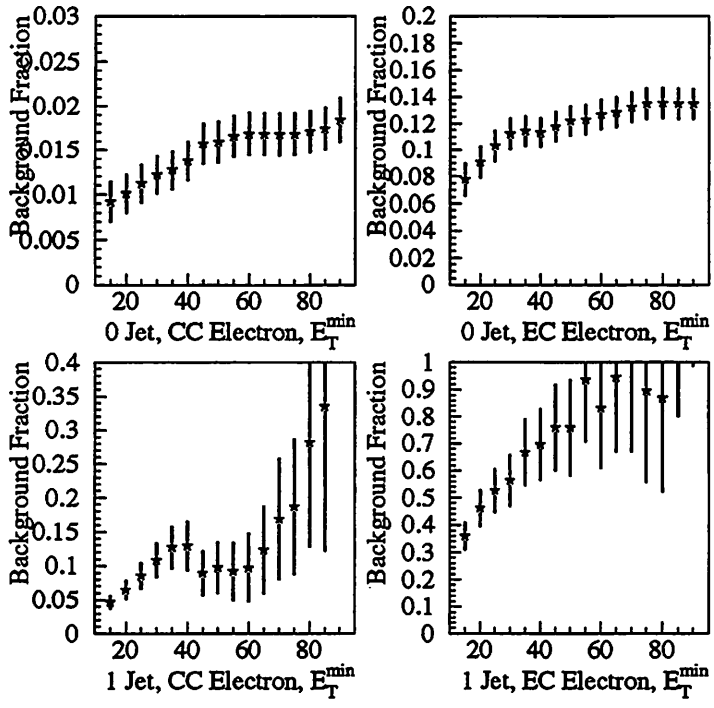

Figure 4.2: Background fraction vs. E_T^{min} for Method 1 – The dip in the 1 Jet CC electron plot is a statistical fluctuation in the background sample in the signal region.

The dependence of the background fractions on E_T^{min} is plotted in Figure 4.2.

Method Two

The reason a second method is needed, other than as a systematic check, has to do with trigger rates, allowed bandwidth, prescales, and statistics. As the instantaneous luminosity increased during the run, it became increasingly difficult to limit the firing rates of triggers and filters to their allowed bandwidths. The solution was to prescale the Level 1 triggers and the Level 2 trigger filters. A prescale of ten meant that only every tenth event which satisfied the trigger was actually kept. As

the instantaneous luminosity increased, the prescales were increased to keep the rate constant. Because of this method of restricting rates, the statistics of many of the high rate triggers (the less restrictive ones) are rather limited, especially at high luminosities.

This is what happened to the background filters for the $W \rightarrow e\nu$ analysis. The overall statistics for these filters is reasonable and the statistics in the normalization region ($\not\!\!E_T <$ 15 GeV) are adequate. However, the limited statistics in the signal region ($\not\!\!E_T >$ 25 GeV) from the background filters would be the source of the dominant error on the background fraction if Method 1 were used.

In order to eliminate the statistics limitation, Method 2 utilizes data from the signal filter as well as the background filters. The method begins the same way as Method 1.

Two samples of data are extracted from the background filters, one with signal and background events ('good' electrons) and the other containing only background events ('bad' electrons). These electromagnetic objects are required to pass the same Level 2 conditions as the electromagnetic objects passing the signal filter. This means that the candidate must pass the Level 2 isolation requirement as well as the shape cuts. This requirement somewhat reduces the statistics in the normalization region but is necessary if the signal filter data is to be used. The normalization factor, M, is then

$$M = \frac{\#\ good\ from\ background\ filter\ with\ \not\!\!E_T < 15\ GeV}{\#\ bad\ from\ background\ filter\ with\ \not\!\!E_T < 15\ GeV}. \qquad (4.4)$$

The next step utilizes the data from the signal filter. Two samples, similar to

the two extracted from the background filters, are extracted from the signal filter using the same two sets of cuts described earlier. One sample contains background and signal ('good' electron) events and the other contains only background ('bad' electron) events. The normalization factor M is then applied to the $\not\!\!E_T$ distribution for the 'bad' sample from the signal trigger.

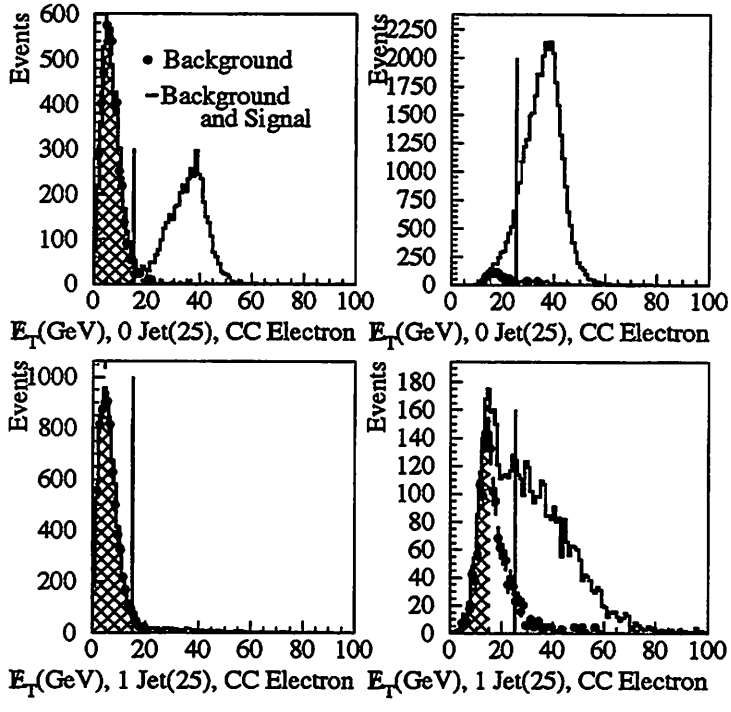

Figure 4.3: Background Subtraction Method 2 – The left hand plots are similar to the plots for Method 1. The right hand plots are for data from the signal filter. The $\not\!\!E_T$ cut in the filter is the reason for the lack of events at low $\not\!\!E_T$ in the right hand plots.

Figure 4.3 is a graphical example of the application of the normalization factor. The left hand plots are similar to the left hand plots in Fig. 4.1 with the vertical line indicating the upper limit for the normalization region. The plots on the right are the $\not\!\!E_T$ distributions for the data from the signal filter. The vertical line here

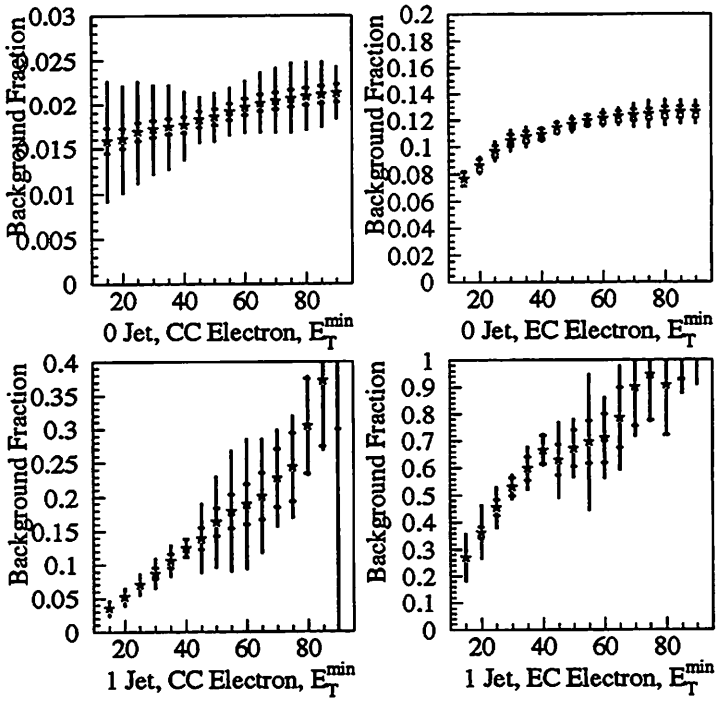

Figure 4.4: Background fraction vs. E_T^{min} for Method 2.

indicates the lower limit for the signal region. The same normalization that was derived from the left hand plots has been applied to the $\not\!\!E_T$ distribution of the 'bad' electrons from the signal filter. The background fraction can be expressed as

$$B.F. = M * \frac{\#\ bad\ from\ signal\ filter\ with\ \not\!\!E_T > 25\ GeV}{\#\ good\ from\ signal\ filter\ with\ \not\!\!E_T > 25\ GeV}. \qquad (4.5)$$

Because the cuts are the same for the data from both sets of filters and because the background fraction is made of internally consistent ratios, all dependence on the amount of luminosity in the samples and on the average instantaneous luminosity of the samples divides out.

The E_T^{min} dependence of these fractions are shown in Figure 4.4. The inner

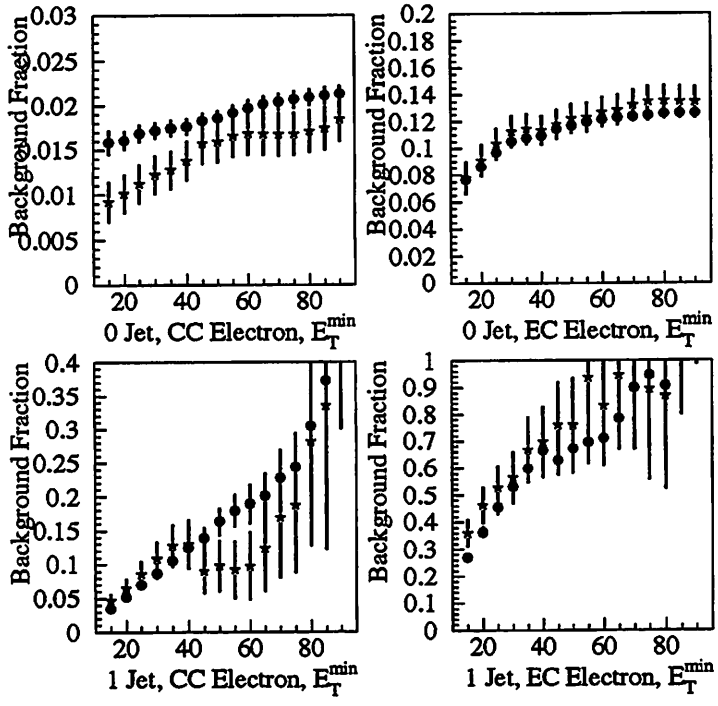

Figure 4.5: Background fraction vs. E_T^{min} for Method 1 and Method 2. The stars are Method 1 and the circles are Method 2. Only statistical errors are shown.

error bars are the statistical errors and the outer error bars are the statistical and the systematic errors added in quadrature. The systematic error in this case is due to the difference between the background fraction from Method 1 and the background fraction measured in Method 2. The magnitude of the systematic error is taken to be the magnitude of the difference between the two methods at each point. Figure 4.5 shows the background fractions for both methods plotted versus E_T^{min}.

Comparison of Method 1 and Method 2

Studying Fig. 4.5 one sees that Method 2 measures a larger multijet background fraction for the $W + 0$ Jets case for central electrons than does Method 1 throughout most of the E_T^{min} range. The trend is the opposite for the $W + 1$ Jet background fractions especially at low values of E_T^{min}. Although no cause for the difference between the two methods could be found, the background fractions from Method 2 are used for the rest of the analysis with the systematic error based on the difference between the two methods.

Tables 4.2 and 4.3 list the background fractions due to multijet events for $W + 0$ Jets and $W + 1$ Jet as a function of E_T^{min} with both statistical and systematic errors.

CC vs. EC

Figures 4.2 and 4.4 plot the background fractions for both CC electrons and EC electrons. The final results of the analysis do not include W candidates with electrons in the EC due to the fact that the background fraction for EC electrons is five to ten times larger than the background fraction for CC electrons. Since the total error on this measurement is not statistics limited (at least for low values of E_T^{min}) the events with electrons in the EC can be eliminated from the sample, resulting in a cleaner sample.

E_T^{min}	CC, 0 Jets BF±stat±syst	EC, 0 Jets BF±stat±syst
15.0	0.01586 ± 0.00138 ± 0.00665	0.07653 ± 0.00535 ± 0.00125
20.0	0.01610 ± 0.00108 ± 0.00597	0.08632 ± 0.00459 ± 0.00462
25.0	0.01688 ± 0.00101 ± 0.00568	0.09693 ± 0.00436 ± 0.00617
30.0	0.01719 ± 0.00095 ± 0.00498	0.10499 ± 0.00427 ± 0.00718
35.0	0.01745 ± 0.00093 ± 0.00471	0.10751 ± 0.00412 ± 0.00691
40.0	0.01762 ± 0.00091 ± 0.00382	0.10922 ± 0.00403 ± 0.00401
45.0	0.01827 ± 0.00092 ± 0.00253	0.11419 ± 0.00406 ± 0.00374
50.0	0.01857 ± 0.00092 ± 0.00264	0.11680 ± 0.00406 ± 0.00534
55.0	0.01919 ± 0.00094 ± 0.00263	0.11952 ± 0.00408 ± 0.00354
60.0	0.01973 ± 0.00095 ± 0.00287	0.12136 ± 0.00409 ± 0.00550
65.0	0.02016 ± 0.00096 ± 0.00334	0.12273 ± 0.00410 ± 0.00579
70.0	0.02041 ± 0.00097 ± 0.00363	0.12373 ± 0.00411 ± 0.00860
75.0	0.02070 ± 0.00097 ± 0.00390	0.12455 ± 0.00412 ± 0.01031
80.0	0.02090 ± 0.00098 ± 0.00381	0.12578 ± 0.00414 ± 0.00969
85.0	0.02110 ± 0.00098 ± 0.00368	0.12634 ± 0.00414 ± 0.00865
90.0	0.02129 ± 0.00099 ± 0.00286	0.12634 ± 0.00414 ± 0.00845

Table 4.2: Multijet background fractions for $W + 0$ Jets for electrons in the CC and the EC.

4.2.2 Direct Photon Backgrounds

Since direct photons are produced in conjunction with a jet they are more likely to affect the $W + 1$ Jet sample than the $W + 0$ Jets sample.

Direct photon events could quite easily fake most of the requirements for the signal sample. A real photon would pass all of the electron requirements except the cut on σ_{track}. Even this can be faked if the photon converts to an electron–positron pair or if a track from another particle happens to point to the calorimeter cluster. The one thing a W event has which a direct photon events should not is a large amount of $\not\!\!E_T$. If a direct photon event does have substantial $\not\!\!E_T$ it is usually due to the Main Ring or some detector effect. Even with the $\not\!\!E_T$cut, there can be some

E_T^{min}	CC, 1 Jet BF±stat±syst	EC, 1 Jet BF±stat±syst
15.0	0.03464 ± 0.00304 ± 0.01190	0.26998 ± 0.01551 ± 0.08931
20.0	0.05183 ± 0.00449 ± 0.01304	0.36319 ± 0.02085 ± 0.09925
25.0	0.07036 ± 0.00618 ± 0.01560	0.45508 ± 0.02725 ± 0.07125
30.0	0.08673 ± 0.00810 ± 0.02168	0.53086 ± 0.03425 ± 0.03359
35.0	0.10557 ± 0.01040 ± 0.02187	0.59884 ± 0.04249 ± 0.06952
40.0	0.12461 ± 0.01310 ± 0.00504	0.66585 ± 0.05219 ± 0.03101
45.0	0.13893 ± 0.01602 ± 0.04900	0.62947 ± 0.05601 ± 0.13017
50.0	0.16315 ± 0.02026 ± 0.06527	0.67233 ± 0.06694 ± 0.08642
55.0	0.17892 ± 0.02461 ± 0.08678	0.69524 ± 0.07833 ± 0.24091
60.0	0.18935 ± 0.02926 ± 0.09196	0.71056 ± 0.09023 ± 0.12092
65.0	0.20098 ± 0.03412 ± 0.07746	0.78480 ± 0.11221 ± 0.16080
70.0	0.22766 ± 0.04273 ± 0.05857	0.89995 ± 0.14607 ± 0.11643
75.0	0.24393 ± 0.05024 ± 0.05689	0.94626 ± 0.17130 ± 0.05185
80.0	0.30507 ± 0.07051 ± 0.02338	0.90705 ± 0.18644 ± 0.03863
85.0	0.37247 ± 0.09796 ± 0.03725	1.21484 ± 0.28572 ± 0.18992
90.0	0.42173 ± 0.12131 ± 0.42173	1.44445 ± 0.37271 ± 0.38889

Table 4.3: Multijet background fractions for $W + 1$ Jet for electrons in the CC and the EC.

contamination in the W signal sample form direct photon events.

This is not a problem if the events are already being removed from the sample. A study comparing the $\not\!\!E_T$ distribution from jet events in which the leading E_T jet has a high electromagnetic fraction, >80%, to the $\not\!\!E_T$ distribution from direct photon candidates with a similar E_T distribution showed that the two distributions have essentially the same shape [14]. Since the $\not\!\!E_T$ of most direct photon events lies in the normalization region of the multijet background subtraction method the conclusion is that this background is being removed with the multijet background.

4.2.3 Electroweak Backgrounds

While multijet events may produce the dominant background for $W(\rightarrow e\nu)$+ Jets production, other electroweak processes can produce events which could fake the signal. These include Drell–Yan and $Z \rightarrow e^+e^-$ events in which one of the electrons is lost between the cryostats or between CC modules so that the events appear to have a single high E_T electron and a large amount of $\not\!\!E_T$. Another source is $Z \rightarrow \tau\tau$ events in which one τ decays electromagnetically and the other τ decays hadronically. These events naturally have $\not\!\!E_T$ due to the neutrinos from the τ decay. These backgrounds were estimated using the ISAJET Monte Carlo [13][15].

Another possible background is $W \rightarrow \tau\nu$ events in which the τ decays to an electron. However, since a W which decays to a τ has as much of a chance to be produced with a jet as a W which decays to an electron, this is not considered to be a background and there is no attempt to remove them from the sample.

For the electroweak background subtraction calculations a luminosity of 75.9 pb^{-1} is used with an error of 10%. This is the source of a small systematic error due to the luminosity measurement in the final result. The number of background events estimated to be in the samples as a function of E_T^{min} are listed in Table 4.4 and Table 4.5.

4.2.4 Backgrounds due to Top Quark Production

A calculation using the current DØ measurement of the top cross section [16] has been done to estimate the background due to top pair production. If all of the top events with only one electron had only one jet that passed an E_T^{min} cut of

E_T^{min}	CC, 0 Jets N±stat±syst	EC, 0 Jets N±stat±syst
20.0	146.5 ± 42.9 ± 14.7	48.6 ± 24.9 ± 4.9
25.0	170.8 ± 48.8 ± 17.1	48.6 ± 24.9 ± 4.9
30.0	171.5 ± 48.8 ± 17.2	50.8 ± 24.9 ± 5.1
35.0	198.8 ± 54.8 ± 19.9	51.6 ± 24.9 ± 5.2
40.0	198.8 ± 54.8 ± 19.9	53.1 ± 24.9 ± 5.3
≥ 45.0	199.6 ± 54.8 ± 20.0	53.1 ± 24.9 ± 5.3

Table 4.4: Number of events due to other electroweak processes in the $W + 0$ Jets samples for both CC and EC electrons. The systematic error is due to the error on the instantaneous luminosity.

E_T^{min}	CC, 1 Jet N±stat±syst	EC, 1 Jet N±stat±syst
20.0	77.4 ± 41.8 ± 7.7	4.5 ± 2.3 ± 0.4
25.0	55.4 ± 34.3 ± 5.5	4.5 ± 2.3 ± 0.4
30.0	53.9 ± 34.3 ± 5.4	2.3 ± 1.5 ± 0.2
35.0	28.1 ± 24.4 ± 2.8	0.7 ± 0.8 ± 0.1
40.0	28.1 ± 24.4 ± 2.8	0.0 ± 0.0 ± 0.0
≥45.0	26.6 ± 24.3 ± 2.7	0.0 ± 0.0 ± 0.0

Table 4.5: Number of events due to other electroweak processes in the $W + 1$ Jet samples for both CC and EC electrons. The systematic error is due to the error on the instantaneous luminosity.

25 GeV, and, assuming the electron would always pass the electron cuts, the top quark background to $W + 1$ Jet would be 2%. Since this is small compared to the other $W + 1$ Jet backgrounds and because it is unlikely that all of the assumptions made above would be true for all candidate events this possible background source is considered to be negligible.

4.2.5 The Effects of High Luminosity or Multiple Interactions

There is a legitimate concern that the multijet background fractions could have a luminosity dependence due to more multiple interactions occurring during high luminosity running.

A tool exists which tags events as probable single or multiple interactions. It has been tuned to data and uses much of the information from the detector to make its determination. For more information about the tool itself see Reference [17].

The multiple interaction tool uses, as part of its input, the amount of energy in the forward calorimetry and the number of vertices which were reconstructed. Because of this the efficiency for the tool to tag a $W + 1$ Jet event as coming from a single interaction is lower than that for it to tag a $W + 0$ Jets event as a single interaction. This is due in part to the amount of energy in the forward calorimeters. Another explanation is that in $W + 1$ Jet events there are more charged particles and therefore more charged tracks than in a $W + 0$ Jets event. An increase in the number of tracks increases the probability for the vertex algorithm to find more than one event vertex which makes it less likely that the multiple interaction tool will tag the event as a single interaction.

In order to be sure that the final result had no dependence on instantaneous luminosity, $\mathcal{L}$, the data set is divided into three luminosity bins with approximately the same amount of data in each bin and the entire analysis is performed on each subset. The luminosity bins are $0 \leq \mathcal{L} < 4.5 \times 10^{30}$, $4.5 \leq \mathcal{L} < 9.25 \times 10^{30}$ and $\mathcal{L} \geq 9.25 \times 10^{30}$. The results for the multijet background fraction and the ratio can

be seen in Figure 4.6 with no corrections made for efficiency differences. While the background fractions display some dependence on the instantaneous luminosity, the final result does not, therefore the data set can be treated as one unit.

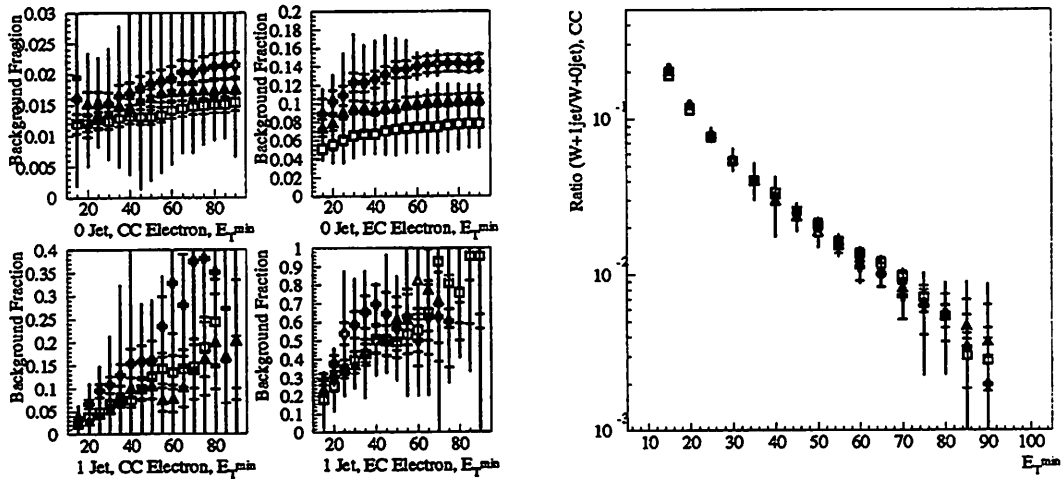

(a) Background Fractions

(b) Ratios

Figure 4.6: Results of instantaneous luminosity study for multijet backgrounds. The squares are the results for low instantaneous luminosities, the triangles are for middle luminosities and the crosses are for high luminosities. No correction has been made for efficiency differences.

The event statistics for $W + 0$ Jets and $W + 1$ Jet after all backgrounds are subtracted are listed in Table 4.6 for $W + 0$ Jets and Table 4.7 for $W + 1$ Jet.

4.3 Z Bosons

To study W detection efficiencies, Z boson events are used. Because the W events in this analysis decay to an electron (positron), the Z events used are those in which the Z decays to an electron–positron pair. In many respects Z events are cleaner

E_T^{min}	CC, 0 Jets Signal±stat±sys	CC, 1 Jet Signal±stat±syst
20	31319.76 ± 184.39 ± 14.67	3731.38 ± 75.40 ± 7.75
25	32878.79 ± 189.81 ± 17.10	2574.53 ± 62.66 ± 5.55
30	33832.70 ± 192.07 ± 17.18	1833.83 ± 56.39 ± 5.40
35	34354.35 ± 194.98 ± 19.91	1396.75 ± 46.30 ± 2.81
40	34707.18 ± 195.82 ± 19.91	1101.17 ± 43.23 ± 2.81
45	34978.67 ± 196.54 ± 19.99	858.62 ± 40.32 ± 2.66
50	35168.04 ± 197.03 ± 19.99	686.43 ± 38.56 ± 2.66
55	35321.32 ± 197.47 ± 19.99	535.87 ± 36.58 ± 2.66
60	35434.27 ± 197.81 ± 19.99	429.83 ± 35.12 ± 2.66
65	35514.57 ± 198.05 ± 19.99	356.16 ± 34.13 ± 2.66
70	35605.30 ± 198.30 ± 19.99	274.65 ± 33.20 ± 2.66
75	35668.16 ± 198.49 ± 19.99	217.64 ± 32.25 ± 2.66
80	35722.44 ± 198.65 ± 19.99	161.06 ± 32.94 ± 2.66
85	35757.44 ± 198.75 ± 19.99	117.76 ± 34.50 ± 2.66
90	35787.55 ± 198.85 ± 19.99	85.62 ± 34.80 ± 2.66

Table 4.6: Signal statistics for $W + 0$ Jets and $W + 1$ Jet for central electrons. The systematic error is only due to the instantaneous luminosity from the electroweak background subtraction.

than W events because both decay products from the Z are easily detected. One simply needs to look for two electrons. As was mentioned earlier, the DØ detector does not not have a central magnetic field so the electron and positron from the decay of the Z look the same in the detector.

4.3.1 Level Ø and Level 1 Triggers

The trigger used for Z events required the Level Ø to fire throughout the entire run. This ensured that all Z candidate events came from an inelastic collision of the proton and the antiproton.

The Level 1 conditions for Z events required that at least two electromagnetic

E_T^{min}	EC, 0 Jets Signal±stat±sys	EC, 1 Jet Signal±stat±syst
20	13888.76 ± 135.10 ± 4.86	1251.24 ± 49.95 ± 0.46
25	14511.59 ± 136.78 ± 4.86	768.15 ± 43.81 ± 0.46
30	14882.36 ± 138.08 ± 5.09	476.71 ± 38.08 ± 0.23
35	15156.50 ± 138.25 ± 5.16	300.91 ± 33.80 ± 0.08
40	15330.72 ± 138.42 ± 5.32	188.79 ± 30.54 ± 0.00
45	15376.82 ± 138.91 ± 5.32	167.48 ± 26.51 ± 0.00
50	15430.24 ± 139.16 ± 5.32	116.00 ± 24.49 ± 0.00
55	15456.58 ± 139.41 ± 5.32	86.25 ± 22.75 ± 0.00
60	15482.93 ± 139.66 ± 5.32	65.12 ± 20.76 ± 0.00
65	15504.43 ± 139.83 ± 5.32	39.38 ± 20.74 ± 0.00
70	15526.04 ± 140.00 ± 5.32	14.11 ± 20.63 ± 0.00
75	15539.51 ± 140.16 ± 5.32	6.13 ± 19.54 ± 0.00
80	15537.62 ± 140.31 ± 5.32	8.83 ± 17.73 ± 0.00
85	15545.20 ± 140.39 ± 5.32	-16.76 ± 22.37 ± 0.00
90	15556.63 ± 140.43 ± 5.32	-29.78 ± 25.23 ± 0.00

Table 4.7: Signal statistics for $W + 0$ Jets and $W + 1$ Jet for central electrons. The systematic error is only due to the instantaneous luminosity from the electroweak background subtraction.

trigger towers have at least 7 GeV of transverse energy deposited in them. The name of the trigger is EM_2_MED.

4.3.2 Level 1.5 Trigger

As the Level 1.5 trigger came on line during the run it was also added to the Z trigger. Only one electromagnetic object was required to pass the E_T cut of 12 GeV and the electromagnetic fraction cut of 85%. These were implemented as they became available as in the case of the W trigger.

4.3.3 Level 2 Filters

Two Level 2 trigger filters are used in the Z studies. Both filters use the same Level 1 trigger conditions discussed above. The less restrictive of the two filters is called EM2_EIS_ESC. This filter required one electromagnetic object to pass the Level 2 isolation and shape cuts that were discussed in the case of the W. That same object must also have a transverse energy of 20 GeV. The other electromagnetic object in the filter was only required to have an E_T of 16 GeV and no cuts were imposed on the isolation or the shower shape.

The second filter used in the Z studies had the same requirements for both of the electromagnetic objects in the event. They both had to pass the Level 2 isolation cut, the shape cut and have an E_T of at least 20 GeV. This filter is called EM2_EIS2_HI.

4.3.4 Offline Cuts

The offline cuts for Z's are similar to the cuts for the W's. For the studies used in this analysis the same event and jet cuts used in the W analysis are made. There is no $\not\!\!E_T$ cut since there is no reason for there to be a neutrino in the event and there is no need to define a 'bad' electron. The Z's do use two levels of cuts on the electron, loose and tight. The difference between the two levels is the number of cuts applied.

A loose electron must satisfy the following criteria:

- identified as a PELC or PPHO,
- E_T greater than 25 GeV,

- $f_{iso} < 0.15$ (Eq. 3.4),
- $EMf > 95\%$ (Eq. 3.1),
- $\chi^2 < 100$ (Eq. 3.3).

A tight electron must pass all of the loose cuts and satisfy two additional requirements:

- identified as a PELC,
- $\sigma_{track} < 5$ if the electron is in the CC and $\sigma_{track} < 10$ if the electron is in the EC (Eq. 3.5).

The final step in identifying Z events is to calculate the invariant mass, M_{12}, from the kinematics of the two electrons

$$M_{12}^2 = (E_1 + E_2)^2 - (\vec{p_1} + \vec{p_2})^2, \tag{4.6}$$

where E_i is the energy of electron i and $\vec{p_i}$ is the momentum of electron i. The signal region is defined as a symmetric distribution around the central value of the LEP measurements for the Z mass.

4.4 Backgrounds in Z Events

Because the mass of the Z is well measured by other experiments, and because both decay products from $Z \rightarrow e^+e^-$ events are detected and measured in the DØ

detector, the background subtraction for the Z events is a little more straightforward than for the W's. For Z's the dielectron mass is plotted and the shape of the distribution is used to estimate the amount of background in the signal region.

Four separate methods are used to estimate the amount of background in the Z signal. One of these simply uses the number of events in different regions of the mass distribution to estimate the amount of background in the signal region. The other three use different fits to the data distribution and estimate the background using different signal windows. They are each described below.

The Side Band Method defines a signal window between 86 and 96 GeV/c^2 in the dielectron mass distribution. Two side band regions are identified as covering 60 to 70 and 110 to 120 GeV/c^2. The number of events in these two regions are averaged and the average is taken to be the amount of background in the signal window. The background fraction is the ratio of the number of background events divided by the total number of events in the signal window. See Figure 4.7.

There are two estimates of the background which use a linear fit for the background shape. They both fit the mass distribution from 70 to 110 GeV/c^2 with a Breit–Wigner convoluted with a Gaussian with a two parameter linear background added to it. The first method uses a signal window of 86 to 96 GeV/c^2 to estimate the background fraction (Figure 4.8(a)). The second method uses a signal window from 81 to 101 GeV/c^2 to estimate the amount of background (Figure 4.8(b)). In both cases the background fraction is the number of events under the linear background fit divided by the total number of events in the signal region.

The last fit method uses the same shape for the mass peak but uses a quadratic form for the shape of the background. The fit window is again from 70 to 110

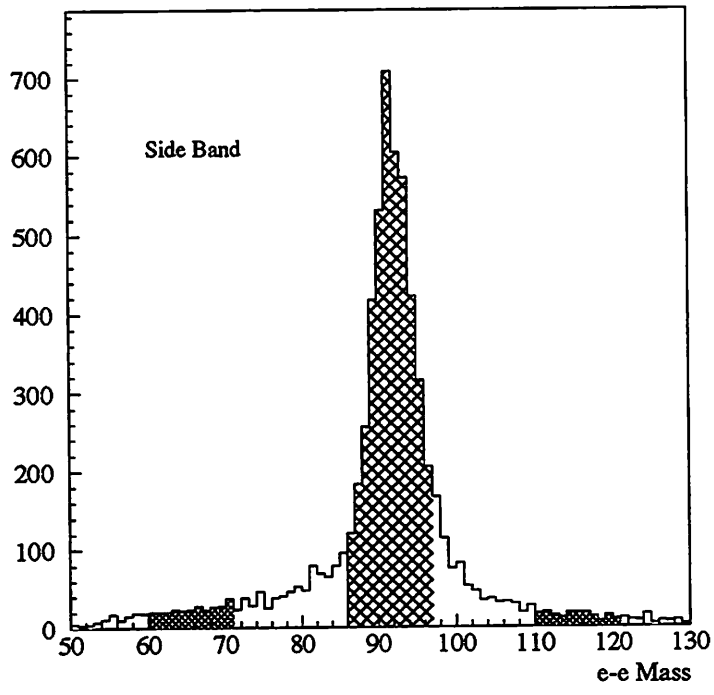

Figure 4.7: Example of the side band method of subtracting background from a Z sample. The shaded regions indicate the side bands and the signal region.

GeV/c^2 and the signal region is defined as 86 to 96 GeV/c^2. The background fraction is then the area under the quadratic fit divided by the number of events in the signal region. See Figure 4.9.

The reason for exploring four different methods is to understand any biases which using only one method could introduce to the estimates.

Much of the work done in this area for this data set was done by Jamal Tarazi [18] at DØ. This analysis simply extended it to treat the different jet multiplicities separately.

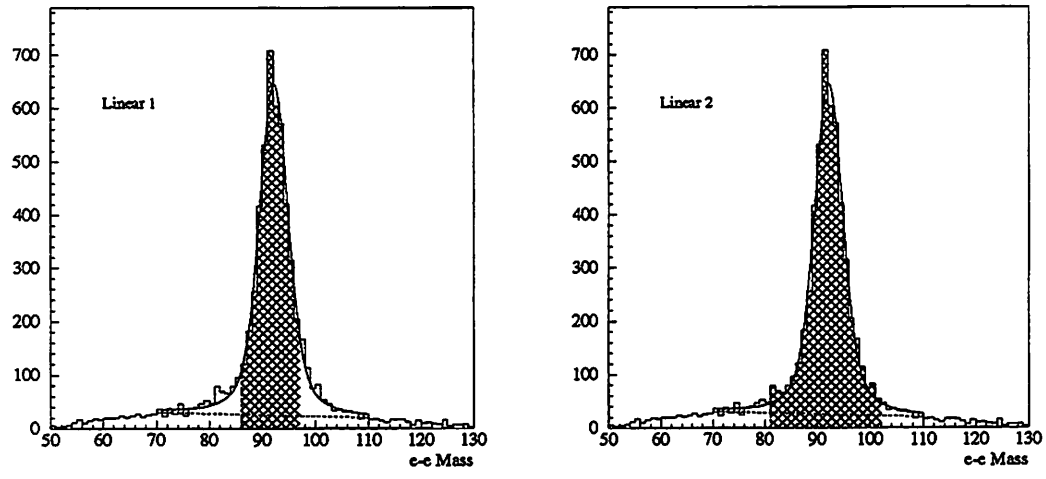

(a) Linear 1

(b) Linear 2

Figure 4.8: Linear background method. The solid curve is the fit to the data. The dashed line is just the linear background part of the fit. Method 2 uses a wider signal window than method 1.

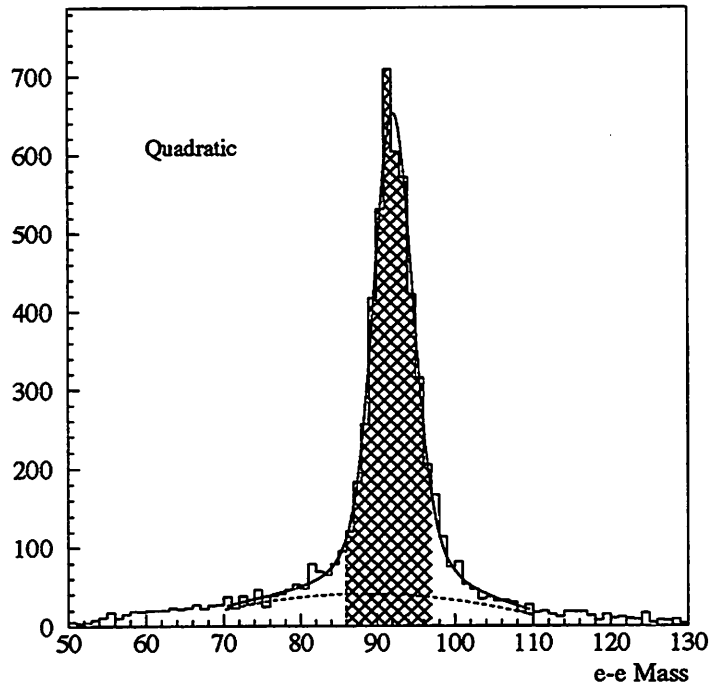

Figure 4.9: Quadratic background subtraction method. The solid curve is the full fit, the dashed curve is just the quadratic part of the fit. This method uses the narrow signal region.

Chapter 5

Corrections to the Data

To compare the results to theoretical predictions, detector and selection effects should be removed from the data as much as possible. Part of these corrections can be classified as a calibration of the detector. Other corrections are made to remove or replace information which the measuring device added to or subtracted from the data. For this analysis most of the corrections are made to the objects reconstructed by DØRECO.

Both the electron candidates and the reconstructed jets have their energies and transverse energies corrected for several effects. These corrections then need to be propagated into the missing E_T, $\not\!\!E_T$, which is the negative of the vector sum of the E_T of all of the objects in the event.

The data must also be corrected for efficiencies. Selection cuts are chosen to be as efficient as possible, but cuts which are 100% efficient allow too much contamination to remain in the data set.

5.1 Electron Corrections

There are two main corrections for electron candidates. One is the energy scale correction for the calibration of the electromagnetic calorimetry. The other correction is for the efficiency of the triggers and offline cuts used to identify an electron candidate.

5.1.1 Electromagnetic Calibration

The calibration for the electromagnetic calorimetry used three different sets of data. The method was the same for each set, identify states which decay into two electromagnetic objects and measure the masses of those states. This was done using π^0 decays [19], J/ψ decays [20], and decays of the Z boson [21]. In the cases of the J/ψ and the Z, the decay products used were electron positron pairs. The π^0 events were selected such that both photons from the π^0 decay converted before they reached the calorimeter.

The electron energy scale also includes corrections due to changed conditions compared to the test beam and corrections for variations in the temperature of the liquid argon [21] [22].

The model used to determine the electromagnetic calibration uses an offset and a multiplicative term. The form is

$$E^{meas} = \alpha_{EM} E^{true} + \delta_{EM} \tag{5.1}$$

where $\alpha_{EM} = 0.9537 \pm 0.0009$ and $\delta_{EM} = -0.16 \pm^{0.03}_{0.21}$ [23].

5.1.2 Electron Cut Efficiencies

As was mentioned in Chapter 1, the strength of a ratio is that many corrections can cancel. To that end, the analysis of electron efficiencies used for the W cross section measurement [18] is repeated with the added jet cuts for this analysis for each jet multiplicity to determine if the electron efficiencies depend on the jet multiplicity or the E_T^{min} cut.

The efficiency for finding an electron can also depend on the instantaneous luminosity regardless of the jet multiplicity or the E_T^{min} cut. Therefore the electron efficiency studies must involve cuts on the instantaneous luminosity as well.

The general method from Ref. [18] is used to measure the efficiency for the Level 2 filter conditions used to identify the electron in the W events and to measure the efficiency of the offline cuts. The measurement is of the efficiency for the cut used to identify the electron and is not an attempt to measure an efficiency curve that can be used in a Monte Carlo simulation.

Electron efficiencies are measured using Z events in the data. The loose Z filter (see Sec. 4.3) is used to select the events. Because this filter only had one electron candidate which was subjected to the full set of cuts the other electron can be used as an unbiased candidate. Since either one of the two electrons has the potential for passing the filter both legs of the Z decay can be used in each event, thereby maximizing the statistics.

The method defines a loose sample and a tight sample. The tight sample differs from the loose by the cut or combination of cuts for which the efficiency needs to be calculated. The efficiency for the cut or set of cuts in question is the number

of events in the signal region in the tight sample divided by the number of events in the loose sample in the signal region [24]. Both of these numbers have the background subtracted from them (see section 4.4).

Since there are four ways to subtract the background from Z events, there are also four ways to measure the electron efficiencies. In order to take advantage of this and to obtain an estimate of the systematic error, all four methods are used. The value used and the statistical error quoted are the measurement closest to the mean of the four measurements and its statistical error, respectively. The systematic error used is the spread of the four measurements. This method was developed for the W cross section measurement [18].

To extend this method to separate jet multiplicities and different values of E_T^{min}, the Side Band Method is dropped for one jet multiplicities due to a lack of statistics in the tails of the mass distribution for $Z + 1$ Jet events.

Efficiency versus Jet Multiplicity and E_T^{min}

The full trigger filter efficiency is measured as well as the efficiencies of the separate components of the electron filter as a function of the number of jets in the event and as a function of the value of the E_T^{min} cut. The separate offline cut efficiencies were also measured in order to understand where any inefficiencies originated. A more detailed discussion of these can be found in Ref. [24]. The result presented here is the full efficiency needed for this analysis. This includes the efficiency for the Level 2 filter and all of the offline cuts.

The efficiency for finding an electron does depend on the jet multiplicity. Figure 5.1 plots the overall efficiency (Level 2 filter plus offline cuts) versus E_T^{min} for

both CC and EC electrons for separate exclusive jet multiplicities. The results for the one jet multiplicity end at an E_T^{min} of 60 GeV due to the fact that the statistics in the Z plus jets sample becomes too small for higher values of E_T^{min} to be useful.

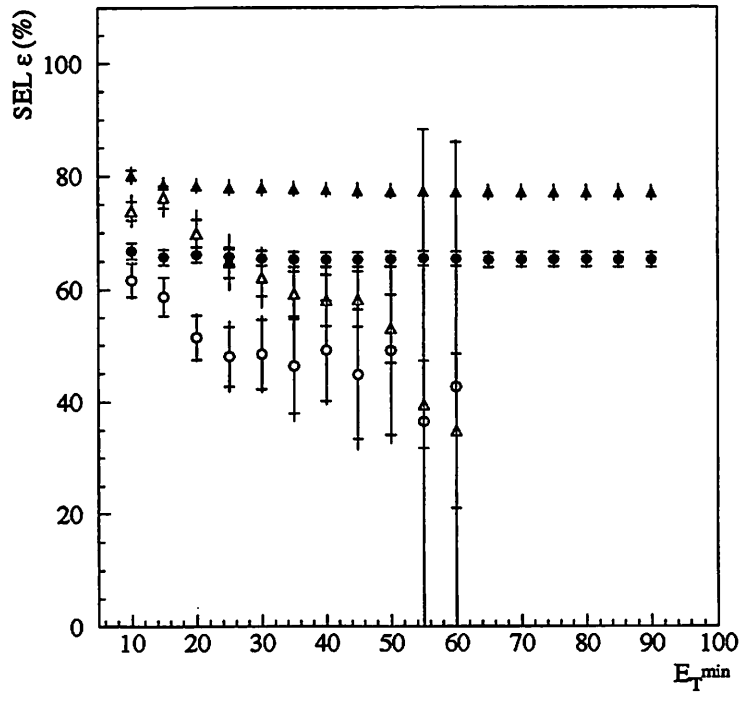

Figure 5.1: Electron efficiencies for exclusive jet multiplicities versus E_T^{min}. The solid symbols are for the zero jet case and the open symbols are for the one jet case. The triangles are for CC electrons and the circles are for EC electrons. The correction factor is the ratio of the solid symbol over the open symbol. The inner error bars are statistical. The outer error bars are statistical and systematic added in quadrature.

The next step is to calculate the correction factor for the measurement of $\mathcal{R}^{10}$ for the electron efficiencies. The correction factor is calculated for central and forward electrons separately. The distributions are plotted versus E_T^{min} in Figure 5.2 and the correction factors for the central electrons are listed in Table 5.1.

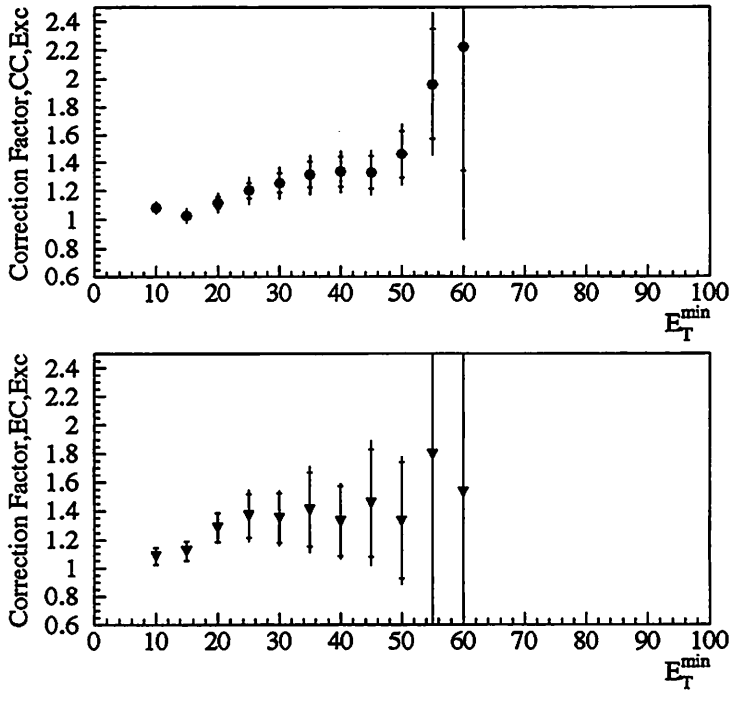

Figure 5.2: Correction factors for $\mathcal{R}^{10}$ versus E_T^{min}. The inner error bar is the statistical error and the outer error bar is statistical and systematic added in quadrature.

Versus Luminosity

The electron efficiencies also depend on the instantaneous luminosity [18]. To measure this for separate jet multiplicities the Z sample is divided into three subsamples as a function of the instantaneous luminosity when the event was triggered. The efficiency measurements are repeated for each subsample. While some of the efficiencies do display a dependence on the instantaneous luminosity (see Fig. 5.3), the dependence is similar for zero jets and one jet events leaving the correction factors, Fig. 5.4, for the ratio flat (within errors) as a function of instantaneous luminosity.

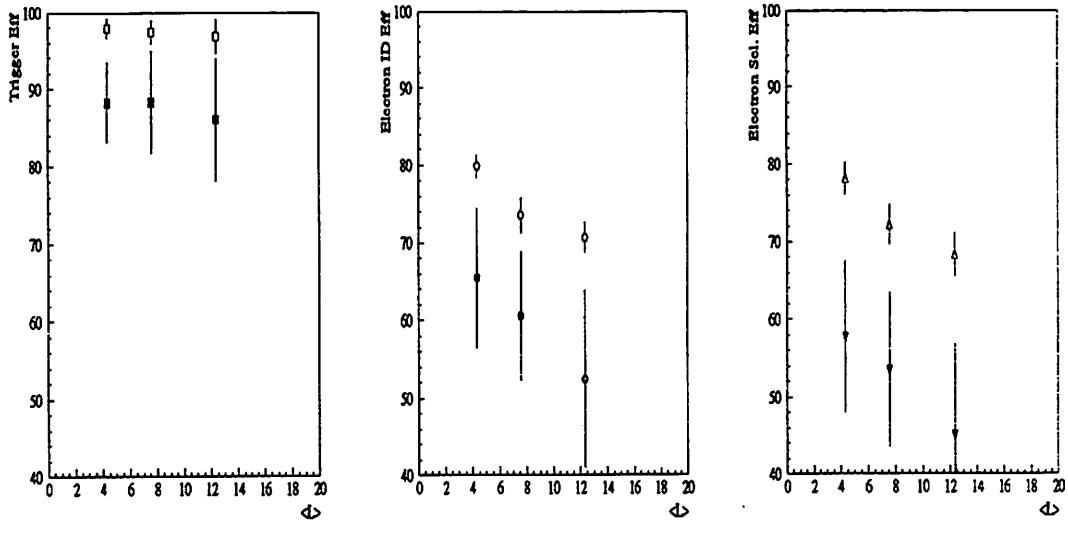

(a) EIS trigger (b) ID efficiency (c) Selection efficiency

Figure 5.3: Electron efficiencies versus luminosity. The open symbols are for the zero jet case and the closed symbols are for the one jet case.

CC versus EC Electrons

Since the efficiencies for EC electrons are lower than the efficiencies for CC electrons and because the errors on the EC electron efficiencies are larger, the EC electrons are not used in the final results.

Table 5.1 lists the correction factors with statistical and systematic errors for $\mathcal{R}^{10}$ with only central electrons as a function of E_T^{min}.

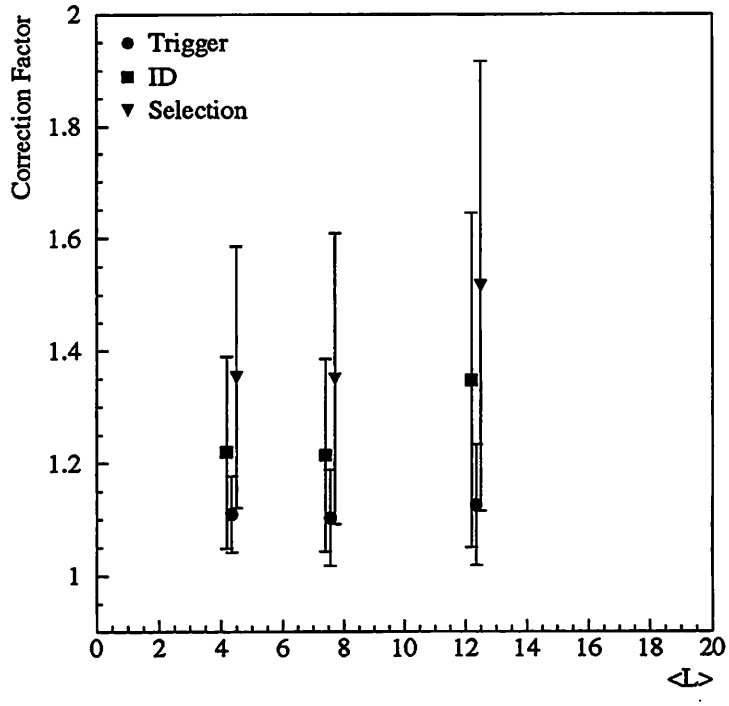

Figure 5.4: Correction factor to the ratio $\mathcal{R}^{10}$ for the various electron efficiencies versus instantaneous luminosity. The selection efficiency is the combined efficiency of the trigger and the offline, or ID, cuts.

5.1.3 Electron Resolutions

While the energy calibration and the cut efficiencies are relatively large corrections the electron energy resolution correction is small in comparison and should cancel in the ratio. It is presented for completeness. The electron energy resolution [21] can be expressed as

$$\frac{\sigma_E}{E} = \sqrt{C^2 + \frac{S^2}{E} + \frac{N^2}{E^2}} \tag{5.2}$$

The parameters C, S and N are derived from test beam data. The value of the sampling parameter, S, is $0.13\sqrt{GeV}$, the constant term, C, is 0.015 and the noise term, N, is 0.4 GeV [21]. This gives a fractional resolution of 3.4% for an electron

E_T^{min}	CF ± stat ± syst
10.0	1.085 ± 0.028 ± 0.037
15.0	1.029 ± 0.028 ± 0.042
20.0	1.119 ± 0.040 ± 0.057
25.0	1.204 ± 0.052 ± 0.080
30.0	1.256 ± 0.066 ± 0.089
35.0	1.314 ± 0.090 ± 0.107
40.0	1.336 ± 0.106 ± 0.102
45.0	1.330 ± 0.114 ± 0.112
50.0	1.459 ± 0.168 ± 0.141
55.0	1.958 ± 0.387 ± 0.323
60.0	2.222 ± 0.881 ± 1.039

Table 5.1: Correction factors due to electron efficiencies for $\mathcal{R}^{10}$ for central electrons. The first error is the statistical error and the second error is the systematic error.

E_T of 25 GeV.

5.2 Jet Energy Scale

The hadronic calorimetry must be calibrated and the corresponding corrections made to the data similar to the case of the electromagnetic calorimetry. The calibration results in the jet energy scale. This scale is more difficult to determine than the electromagnetic and also depends on the electromagnetic scale. A more detailed description of the corrections and the method used to determine them can be found in Reference [25].

The jet energy scale is used to correct jets, on average, back to the particle level, or the point where the colored parton has become a noncolored object. The correction first removes energy in the jet which is not from the hard interaction

which produced the jet. This is called the offset correction, O. The jet is then corrected for the response of the hadronic calorimeter, R, to energy deposited in it. The final jet correction depends on the algorithm used to define a jet and corrects for showering effects, S. The particle jet energy takes the form

$$E^{jet}_{particle} = \frac{E^{jet}_{measured} - O}{(1-S)R} \tag{5.3}$$

The offset correction removes two types of energy deposition. The first is energy deposited in the jet by beam remnants or secondary interactions in the same beam crossing. The other part of the correction corrects for noise. Sources of noise include electronic noise from the readout and ionization from the decay of uranium nuclei in the calorimetry.

The response correction is responsible for correcting the energy of the jet for all effects not related to the algorithm used to define a jet. This includes corrections due to changes in the scale relative to the test beam data, differences in scale due to the different detectors in the calorimetry, inefficiencies in the reconstruction of low E_T jets and impurities and temperature variations in the liquid argon.

The response correction is derived from the data. Direct transverse energy balancing is not used so as not to bias other jet measurements. An adaptation of the "Missing E_T Projection Method" or MPF is used [25]. In this method the $\not\!\!E_T$ is projected onto the direction of a trigger object. The response, R, can be expressed as

$$R = 1 + \frac{\vec{\not\!\!E}_T \cdot \hat{n}^{trigger}_T}{E^{trigger}_T}. \tag{5.4}$$

where $\hat{n}$ is the direction of the trigger object.

Two types of events are used to determine R, dijet events and photon plus jets events. The advantage of the photon data is that the photon, which is used as the trigger object, is well measured in the electromagnetic calorimetry and the electromagnetic energy scale is well determined (Section 5.1.1). The observable used to measure R is E' which is defined as

$$E' = E_T^{\gamma} \cosh(\eta_{jet}). \tag{5.5}$$

Since both E_T^{γ} and η_{jet} are well measured the observable has a good resolution.

While the photon data is well anchored by the electromagnetic scale it does not have data at very high jet E_T's. The dijet data used to measure the response provide a wide reach in jet E_T's. In this case one jet is chosen as the trigger object and the other is the jet referred to in equation 5.5. This data cannot provide an absolute measurement of the response since the cuts used to select the events can bias the $\not\!\!E_T$. This bias manifests itself as a change in the overall normalization. In this case only the relative dependence of R on E' is important and the bias is normalized away [25].

The final correction to the jets must be determined for each jet algorithm separately. This is the showering correction. This correction attempts to replace the energy of the particle lost by the clustering algorithm due to the hadron showering. The determination of this correction uses HERWIG Monte Carlo overlayed with calorimeter particle showers from test beam data. This combination is used to measure the amount of a particle's energy which is in the calorimeter but that is not clustered by the jet algorithm. This is a small correction for a cone with a

radius of 0.7 [25].

The order of the corrections to jet energies is:

1. correct reconstructed electromagnetic clusters
2. remove reconstructed electromagnetic clusters from jets
3. apply the low E_T bias correction
4. apply offset corrections
5. apply detector scale corrections
6. apply absolute hadronic scale
7. apply showering correction
8. replace corrected electromagnetic clusters

The final step in the energy scale corrections is to correct the $\not\!\!E_T$ in the event for the changes made to the electromagnetic and hadronic objects in the event.

5.2.1 Energy Scale Errors

All of the jet energy scale corrections have an error associated with them. The relative correction to jets ranges from -5% to +20% as a function of the jet E_T with errors of 3-4% [25] of the jet E_T. This is a large error and can have a visible impact on the measurement of $\mathcal{R}^{10}$, mainly because the corrections not only affect the jets but also the $\not\!\!E_T$. This has an impact on the selection of signal events.

To determine the impact of the jet energy scale errors on this measurement, the analysis of the data is repeated three times, once with the nominal jet corrections, once with the nominal correction $+1\sigma$, and once with the nominal correction -1σ. All jet cuts are applied after the corrections. The changes in the jet E_T's are propagated into the $\not\!\!E_T$ and the full event selection and multijet background subtraction was repeated. Figure 5.5 shows how jet E_T's are affected by the variation. The solid histogram is the E_T distribution of the leading E_T jet (with an E_T^{min} cut of 25 GeV imposed) after the nominal corrections have been applied. The dashed histogram is the nominal $+1\sigma$ and the dotted histogram is nominal -1σ.

Figure 5.6 shows how the $\not\!\!E_T$ is affected by the corrections. The solid histogram is the $\not\!\!E_T$ distribution after the nominal jet correction has been applied to each jet in the event and then propagated into the $\not\!\!E_T$ calculation. The dashed histogram is the $\not\!\!E_T$ after the jet E_T's have been corrected to nominal $+1\sigma$ while the dotted histogram is the $\not\!\!E_T$ after the jets have been corrected to nominal -1σ.

The result is that the high jet corrections produce a higher value of $\mathcal{R}^{10}$ and the low jet correction a lower measurement of $\mathcal{R}^{10}$. The difference between the nominally corrected $\mathcal{R}^{10}$ and the high corrected $\mathcal{R}^{10}$ is taken to be the positive systematic error on the ratio due to the jet energy scale errors and the difference in $\mathcal{R}^{10}$ between the nominal and low corrections it taken to be the negative error. These errors are plotted versus E_T^{min} in Figure 5.7 for $\mathcal{R}^{10}$ using only central electrons. For E_T^{min} greater than 50 GeV the statistical errors on the ratio become large and the error due to the jet energy scale errors is not well determined due to statistical fluctuations.

The ratio, $\mathcal{R}^{10}$, as a function of E_T^{min} is listed in Table 5.2 for central and forward

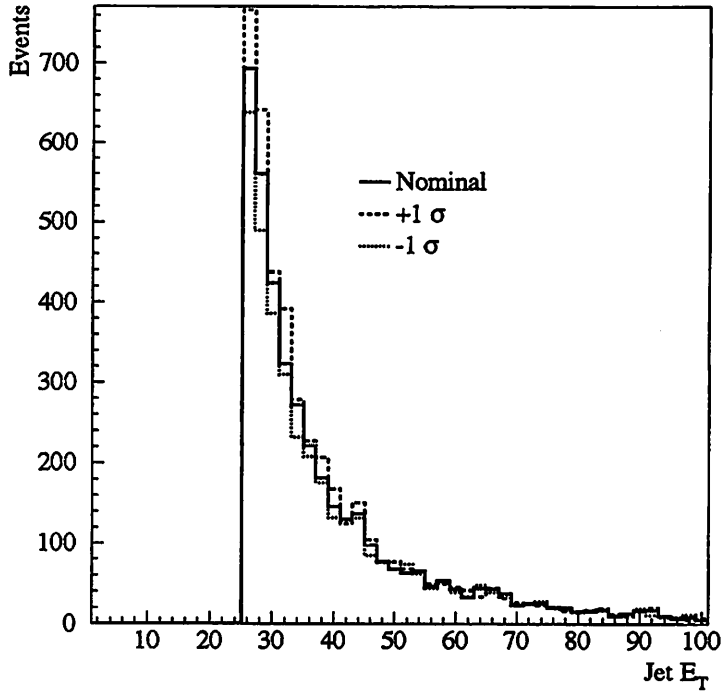

Figure 5.5: Transverse energy distributions of the leading jet for an E_T^{min} of 25 GeVfor the nominal, nominal $+1\sigma$ and nominal -1σ jet energy scale corrections.

electrons with systematic errors due to the jet energy scale but no corrections made for efficiencies. No ratio is listed for EC electrons for an E_T^{min} of 85 and 90 GeV because the multijet background fractions for these were greater than 100% (see Table 4.3).

5.3 Jet Energy Resolution

The jet energy scale corrections, which attempt to correct the jet energies back to the particle level, only correct the jets by the average correction. However, the jet energies are still smeared due to the finite resolution of the hadronic calorime-

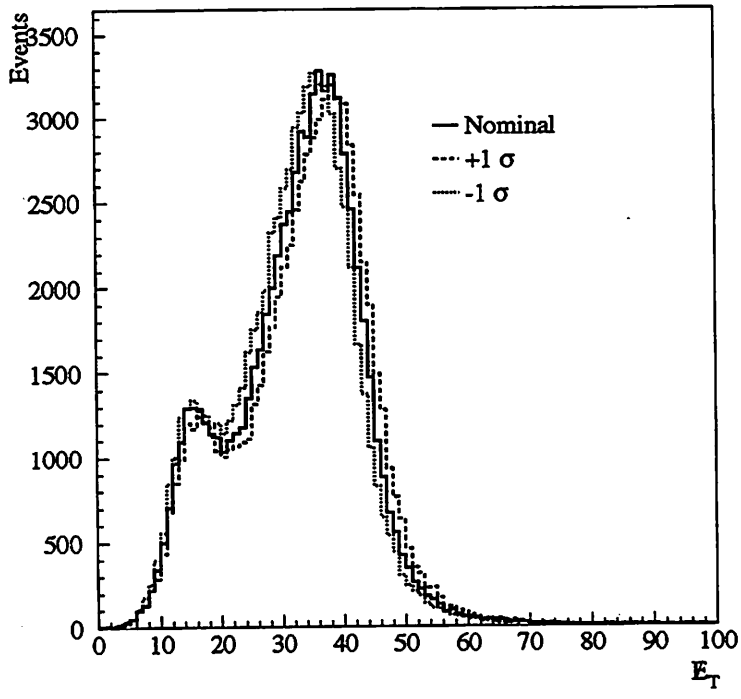

Figure 5.6: The $\not\!\!E_T$ distributions for the signal sample for the nominal, nominal $+1\sigma$ and nominal -1σ jet energy scale corrections.

try [26]. The resolution can be parameterized as

$$\frac{\sigma_E}{E} = \sqrt{\frac{N^2}{E^2} + \frac{S^2}{E} + C} \tag{5.6}$$

where C is a constant offset and $\frac{S}{\sqrt{E}}$ represents smearing due to sampling fluctuations, intrinsic energy resolution of the calorimetry and detector imperfections. The $\frac{N}{E}$ term is the smearing due to noise fluctuations. Since the CC, the EC's and the intercryostat region contain different detectors, different resolutions should be expected in different regions of the detector.

The resolutions were measured [26] using a dijet asymmetry method in which

- the E_T of the jets must be greater than 15 GeV,

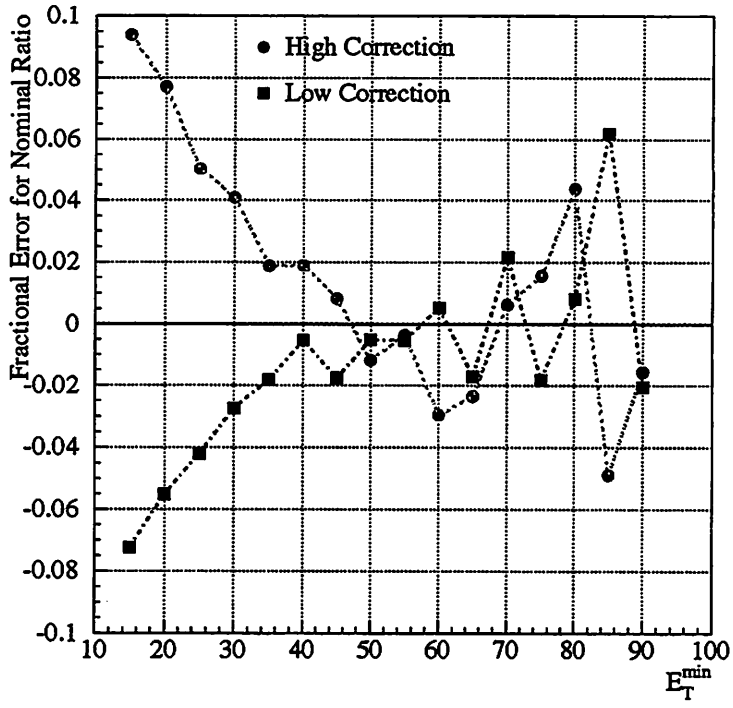

Figure 5.7: Fractional error on $\mathcal{R}^{10}$ due to the jet energy scale errors for central electrons only.

- the jets must be back to back in ϕ (within 5°),
- the jets must be in the same $|\eta|$ region, and
- no other reconstructed jets with an E_T greater than 8 GeV are present in the event.

Since jet measurements are based on the E_T of the jet, it is actually the E_T resolution $\frac{\sigma_{E_T}}{E_T}$ which is measured as a function of jet E_T. The resolution parameters for different η regions are listed in Table 5.3. In this analysis the data is not corrected for these resolutions. Instead, the theoretical predictions have been smeared. This will be discussed more in Section 6.1.

E_T^{min}	CC $R^{10}\pm$stat$\pm$syst	EC $R^{10}\pm$stat$\pm$syst
20.0	$0.1191 \pm 0.0025 \pm^{0.0095}_{0.0069}$	$0.0901 \pm 0.0037 \pm^{0.0073}_{0.0075}$
25.0	$0.0783 \pm 0.0020 \pm^{0.0042}_{0.0036}$	$0.0529 \pm 0.0031 \pm^{0.0050}_{0.0055}$
30.0	$0.0542 \pm 0.0017 \pm^{0.0026}_{0.0020}$	$0.0320 \pm 0.0026 \pm^{0.0129}_{0.0130}$
35.0	$0.0407 \pm 0.0014 \pm^{0.0013}_{0.0013}$	$0.0198 \pm 0.0022 \pm^{0.0153}_{0.0152}$
40.0	$0.0317 \pm 0.0013 \pm^{0.0007}_{0.0003}$	$0.0123 \pm 0.0020 \pm^{0.0190}_{0.0190}$
45.0	$0.0245 \pm 0.0012 \pm^{0.0014}_{0.0015}$	$0.0109 \pm 0.0017 \pm^{0.0158}_{0.0159}$
50.0	$0.0195 \pm 0.0011 \pm^{0.0016}_{0.0016}$	$0.0075 \pm 0.0016 \pm^{0.0145}_{0.0145}$
55.0	$0.0152 \pm 0.0010 \pm^{0.0017}_{0.0017}$	$0.0056 \pm 0.0015 \pm^{0.0107}_{0.0107}$
60.0	$0.0121 \pm 0.0010 \pm^{0.0015}_{0.0015}$	$0.0042 \pm 0.0013 \pm^{0.0249}_{0.0249}$
65.0	$0.0100 \pm 0.0010 \pm^{0.0011}_{0.0011}$	$0.0025 \pm 0.0013 \pm^{0.1621}_{0.1621}$
70.0	$0.0077 \pm 0.0009 \pm^{0.0006}_{0.0007}$	$0.0009 \pm 0.0013 \pm^{0.1269}_{0.1269}$
75.0	$0.0061 \pm 0.0009 \pm^{0.0005}_{0.0005}$	$0.0004 \pm 0.0013 \pm^{0.1058}_{0.1058}$
80.0	$0.0045 \pm 0.0009 \pm^{0.0003}_{0.0002}$	$0.0006 \pm 0.0011 \pm^{0.0242}_{0.0242}$
85.0	$0.0033 \pm 0.0010 \pm^{0.0003}_{0.0003}$	
90.0	$0.0024 \pm 0.0010 \pm^{0.0023}_{0.0023}$	

Table 5.2: $\mathcal{R}^{10}$ for central and forward electrons as a function of E_T^{min} with no efficiency corrections. The systematic error includes the error due to the jet energy scale errors.

5.4 $\not\!\!E_T$

The $\not\!\!E_T$ of an event is measured using the vector E_T balance of the transverse energy in the calorimeter. Because of this the $\not\!\!E_T$ must be corrected for all corrections made to the rest of the energy in the calorimeter to maintain the balance. This also means that the resolution of the $\not\!\!E_T$ measurements are only as good as the resolutions of the other objects in the event.

η Range	N	S	C
$\lvert\eta\rvert < 0.4$	3.848	0.539	0.027
$0.4 \leq \lvert\eta\rvert < 0.8$	4.789	0.423	0.041
$0.8 \leq \lvert\eta\rvert < 1.2$	3.067	0.635	0.047
$1.2 \leq \lvert\eta\rvert < 1.6$	4.654	0.349	0.055
$1.6 \leq \lvert\eta\rvert < 2.0$	3.484	0.556	0.000
$2.0 \leq \lvert\eta\rvert < 3.0$	3.729	0.428	0.000

Table 5.3: Jet resolution parameters.

5.4.1 $\not\!\!E_T$ Corrections

The first calculation of the $\not\!\!E_T$ in the event is made using the uncorrected energy in the calorimetry. Therefore any changes to the energy of the objects in the event must be propagated into the $\not\!\!E_T$. This is done for corrections made to all electron, photon, jet and muon candidates. All $\not\!\!E_T$ cuts in this analysis are made on a $\not\!\!E_T$ that has been corrected for all of the above except muons.

5.4.2 $\not\!\!E_T$ Efficiency

The efficiency of the $\not\!\!E_T$ cut used to define the signal sample depends on the objects in the event. Since the resolution of the electromagnetic calorimetry is better than that for the hadronic the resolution for $\not\!\!E_T$ measurements is better in events with a high E_T electromagnetic object than those without one. This difference in resolution directly affects the efficiency of the $\not\!\!E_T$ cut used to define the signal region.

The $\not\!\!E_T$ efficiency is measured using the background filters for W's (see Section 4.1.3). These did not have a $\not\!\!E_T$ cut in them and are therefore unbiased. The efficiency is measured for both 'good' and 'bad' electrons, as defined in Sec-

tion 4.1.4, separately for the central and end cryostats and for separate jet multiplicities as a function of E_T^{min}.

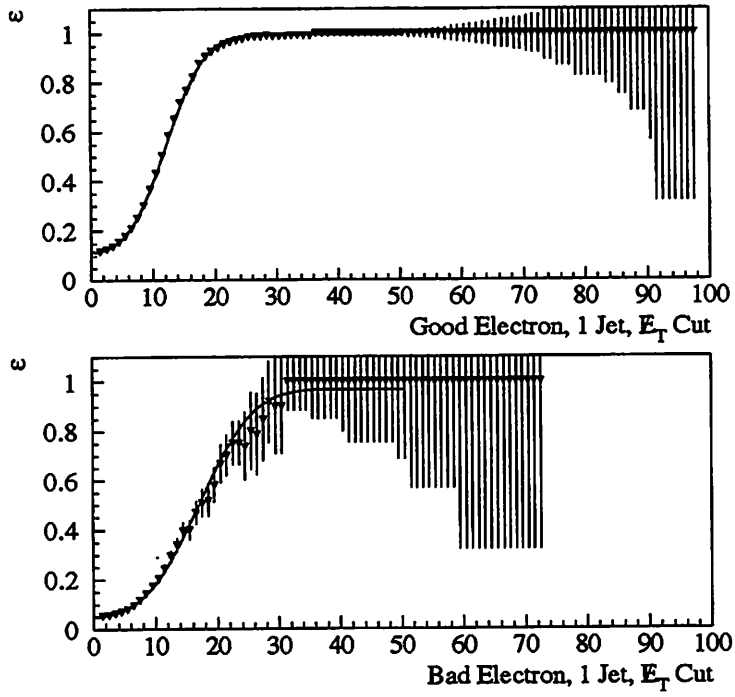

Figure 5.8: Examples of $\not\!\!E_T$ cut efficiency curves. Each point is the integrated efficiency from the value of $\not\!\!E_T$ at which it is plotted to infinity, giving the efficiency for a cut on the $\not\!\!E_T$ at that point.

The method is straightforward. The corrected $\not\!\!E_T$ distribution is plotted first with no requirement on the Level 2 $\not\!\!E_T$. A cut of 15 GeV is then made on the $\not\!\!E_T$ measured by the Level 2 algorithm. This is the value of the cut which was in the signal filter. The distribution with the Level 2 $\not\!\!E_T$ cut is then divided by the distribution without the cut. The resulting curve gives the efficiency for the $\not\!\!E_T$ with a Level 2 requirement imposed. The measurement needed is the efficiency for a cut which selects events with $\not\!\!E_T$ greater than N GeV. To do this the efficiency

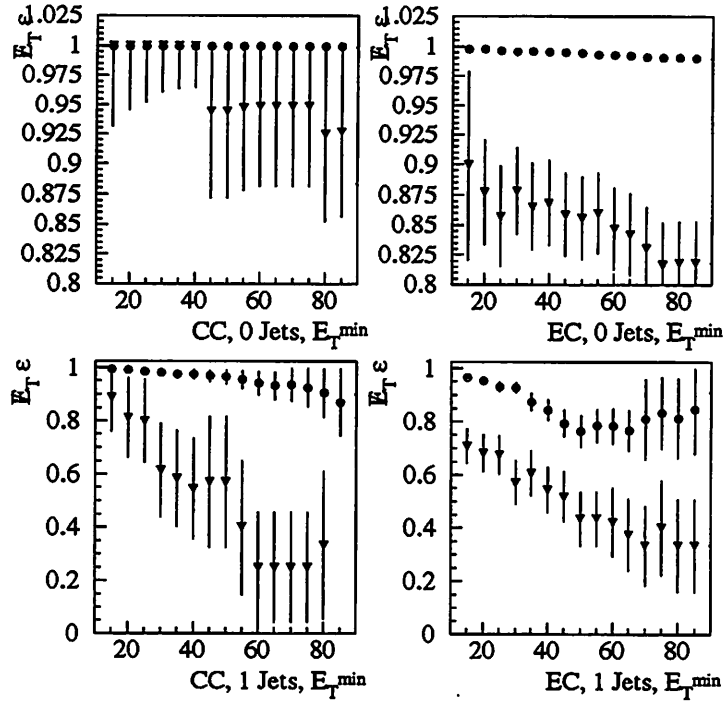

Figure 5.9: $\not\!\!E_T$ efficiencies versus $E_T^{min}$for $\not\!\!E_T$ greater than 25 GeV. The circles are the $\not\!\!E_T$ efficiency when there are good electrons in the events and the triangles are for bad electrons.

curve must be integrated from N GeV to infinity. Figure 5.8 has examples of the integrated curves for jet multiplicities of one with an E_T^{min} cut of 25 GeV on the jets for good and bad electrons in the central calorimetry.

Figure 5.9 plots the cut efficiency for an offline $\not\!\!E_T$ cut of 25 GeV as a function of E_T^{min} for good and bad electrons in the CC and the EC for the zero jet and one jet multiplicities. The $\not\!\!E_T$ cut efficiency for good electrons in the CC is the same within errors regardless of the jet multiplicity or the value of E_T^{min}. There is a slight decrease in the $\not\!\!E_T$ efficiency for good electrons in the CC when there is a jet in the event as a function of E_T^{min} but it is accompanied by an increase in

the size of the error bars. The correction factor from the different $\not\!\!E_T$ efficiency for good electrons in the CC is plotted in Figure 5.10 and the values of the correction factors are listed in Table 5.4.

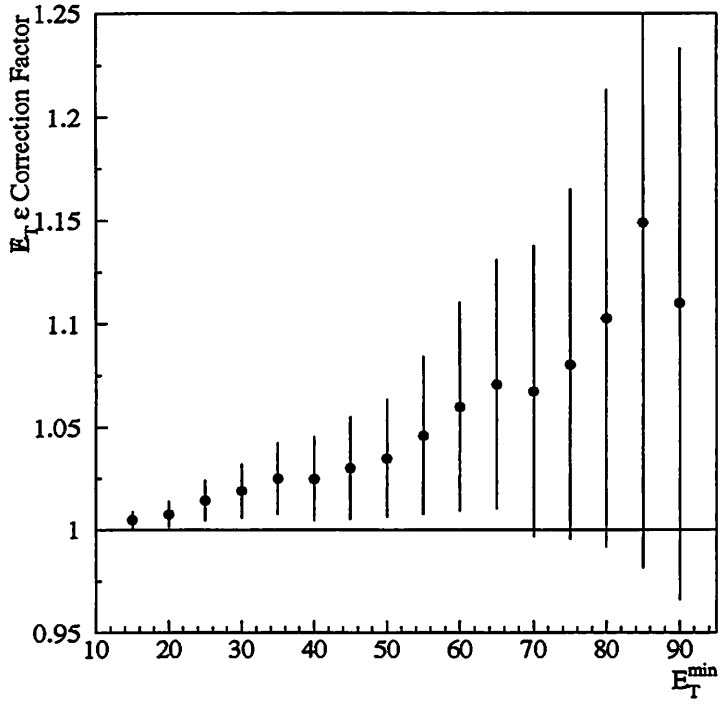

Figure 5.10: Correction factors for $\mathcal{R}^{10}$ due to $\not\!\!E_T$ efficiencies versus E_T^{min}.

The $\not\!\!E_T$ cut efficiency for events with a 'bad' electron is substantially lower than for that a good electron when there is a jet in the event and decreases as a function of E_T^{min}. At first glance this indicates the need for a correction to the multijet background fractions from Method 2 (section 4.2.1). In fact this indicates that the Level 2 $\not\!\!E_T$ cut rejects some of the multijet (and direct photon) background which could have been in the sample.

There is a possibility that the multijet backgrounds are slightly overestimated in Method 2 since the normalization factor does not take into account the rejection

E_T^{min}	CF + high stat − low stat
15.0	1.0048 + 0.0043 − 0.0043
20.0	1.0075 + 0.0064 − 0.0064
25.0	1.0141 + 0.0100 − 0.0100
30.0	1.0189 + 0.0134 − 0.0134
35.0	1.0249 + 0.0176 − 0.0176
40.0	1.0248 + 0.0206 − 0.0206
45.0	1.0301 + 0.0251 − 0.0251
50.0	1.0347 + 0.0289 − 0.0289
55.0	1.0458 + 0.0384 − 0.0384
60.0	1.0599 + 0.0508 − 0.0508
65.0	1.0707 + 0.0604 − 0.0604
70.0	1.0672 + 0.0707 − 0.0707
75.0	1.0801 + 0.0851 − 0.0851
80.0	1.1025 + 0.1109 − 0.1109
85.0	1.1490 + 0.1675 − 0.1675
90.0	1.1099 + 0.1233 − 0.1442

Table 5.4: Correction factors for $\not\!\!E_T$ efficiency corrections to $\mathcal{R}^{10}$ for central electrons. The first error is the high statistical error and the second error is the low statistical error.

of the background by the Level 2 $\not\!\!E_T$ cut. This may explain some of the difference between the background fractions measured in Method 1 and Method 2. The difference is already covered by the errors.

Chapter 6

Results and Comparisons to Theory

At this point the data has been corrected for the background contamination and selection efficiencies, and the jets have been corrected back to the particle level. The events have not been corrected for the resolution of the hadronic calorimetry or the acceptance of the fiducial coverage of the detector. These last two major effects are incorporated into the theoretical calculations used to compare to the measurement.

6.1 Theory

The theoretical calculations used in this study use the DYRAD Monte Carlo by Giele, Glover and Kosower [7]. This is a next-to-leading order calculation, in terms of α_s, for $W + 0$ Jets and $W + 1$ Jet which includes interference with loop

diagrams. NLO in α_S means that $W + 0$ Jets includes terms proportional to α_S and $W + 1$ Jet includes terms proportional to α_s^2. The Monte Carlo is capable of calculating either the inclusive cross sections, $W+ \geq N$ Jets, or the exclusive $W + N$ Jets for $N = 0, 1$. For this analysis DYRAD was used in its exclusive mode.

One of the strengths of the DYRAD Monte Carlo is that the 4-vectors of the final state partons are accessible so that the same cuts applied to the data can be applied to the theory and then the prediction for the cross section is made. The Monte Carlo is also capable of only using the particles within the same fiducial volume as the detector to calculate the $\not\!\!E_T$ or to count the jets. There is no fragmentation of the final state partons but they can be clustered into 'jets' using the same algorithm as the data. Recall that the NLO correction for $W + 1$ Jet includes $W + 2$ Jets where the two partons cannot be resolved, one of the partons fails the E_T^{min} cut, or one of the partons goes outside of the detector coverage. This enable the Monte Carlo to incorporate the acceptance of the detector in the calculation.

The jet resolutions discussed in Section 5.3 are used to smear the energies of the Monte Carlo 'jets' to match the smearing of the detector. A cut is also made on the distance in η-ϕ space between the electron and the jets in the event to model the isolation cut imposed on the electron in the data and the acceptances (geometric and kinematic) for electron plus jet events. Once all of this is done the Monte Carlo calculation and the data are on the same level.

6.1.1 W Production and Decay

The calculation for the W production and decay is based on calculations for the production of a vector boson from the interaction of two leptons. The vector boson is then allowed to decay into a quark-antiquark pair. To apply this calculation to W production from $\bar{p}p$ interactions the initial and final state partons are crossed such that the vector boson is produced by the quark-antiquark interaction and the vector boson decays into a lepton pair [7].

6.1.2 Jet Clustering

The challenge for clustering Monte Carlo partons is to do it in such a way that the data algorithm and the Monte Carlo algorithm are doing the same thing. A great deal of time was spent studying this at DØ [27]. What is used in the Monte Carlo is a modified Snowmass [28] algorithm.

The Snowmass algorithm clusters partons together when they are within a distance R in η-ϕ space of the 'jet' axis which is defined as

$$\eta_{jet} = \frac{\sum_i E_T^i \eta^i}{\sum_i E_T^i} \tag{6.1}$$

$$\phi_{jet} = \frac{\sum_i E_T^i \phi^i}{\sum_i E_T^i} \tag{6.2}$$

where the $\sum_i$ is a sum over the partons in the jet. This can produce Monte Carlo jets in which two partons which are separated by a distance $2 \times R$ are clustered into one jet.

In studies comparing jets in the DØ calorimeter to NLO Monte Carlo jets [27]

it was found that this algorithm did not reproduce the jet direction distributions observed in the data. The parameter, R_{sep}, was introduced to restrict the distance between partons in a jet to a separation of $R_{sep} \times R$. For the unmodified Snowmass algorithm R_{sep} is 2. DØ found that using a value of 1.3 for R_{sep} brought the Monte Carlo jets into agreement with the data [27]. This algorithm is used in the theoretical calculations used for this analysis.

6.1.3 Monte Carlo Inputs

As was discussed in Chapter 1, the calculations for W production at a $\overline{p}p$ collider need to use the parton distribution functions, PDF's, of the proton as inputs. This is true for any theoretical calculation for hadron colliders since hadrons are composite particles.

One parameter in the fits which produce the PDF's is Λ_{QCD}. Because Λ_{QCD} and α_s are related, each PDF fit has one value of $\alpha_s(M_W^2)$ associated with it. Therefore any calculation using that PDF has a specified value of $\alpha_s(M_W^2)$. If a calculation is needed with a different value of $\alpha_s(M_W^2)$ a different PDF must be used. Several PDF families have been produced in which Λ_{QCD} has been varied in the fits.

Two families of PDF's are used in the comparison of data and theory. One is the CTEQ4 family [29] and the other is the MRSA family [30]. Each family comes with a preferred fit, CTEQ4M and MRSA'. Each member of these families is used in the calculations which follow.

6.2 $\mathcal{R}^{10}$ vs. E_T^{min}

As was mentioned before, only electrons in the Central Calorimeter are used in the final results. Electrons in the EC have higher backgrounds and lower efficiencies.

The E_T cut on the jets is varied in the analysis to study the dependence of $\mathcal{R}^{10}$ on E_T^{min} and to determine whether the theoretical calculation and the experimental measurement have the same shape. Figure 6.1 plots the measured ratio as a function of the value of E_T^{min} (the circles). The inner error bars, where they can be seen, are the statistical errors on the ratio and the outer error bars are the statistical and the systematic added in quadrature. The E_T^{min} range shown does not include the 15 GeV point due to inefficiencies in the jet reconstruction for low E_T jets [31]. Points for E_T^{min} greater than 60 GeV are not included because of the low statistics in the electron efficiency measurement for E_T^{min}>60 GeV.

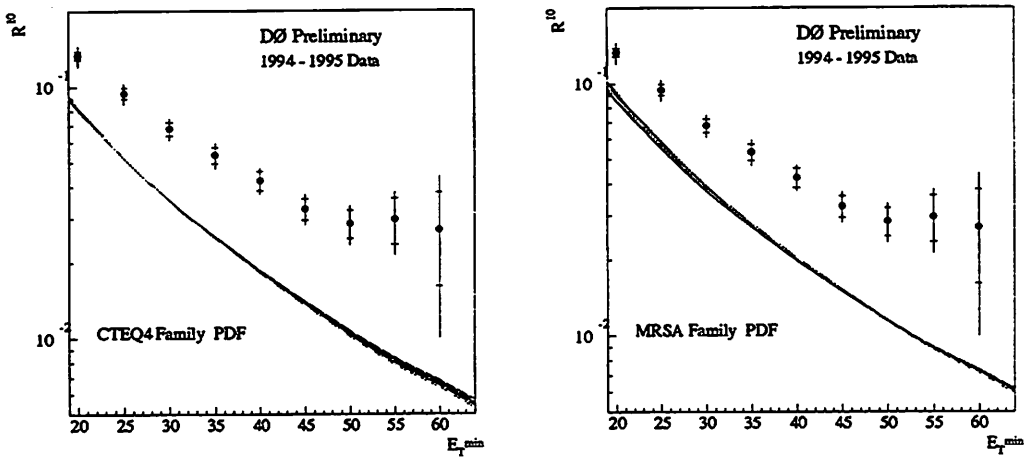

Figure 6.1: $\mathcal{R}^{10}$ versus E_T^{min} with the CTEQ4 and MRSA PDF families.

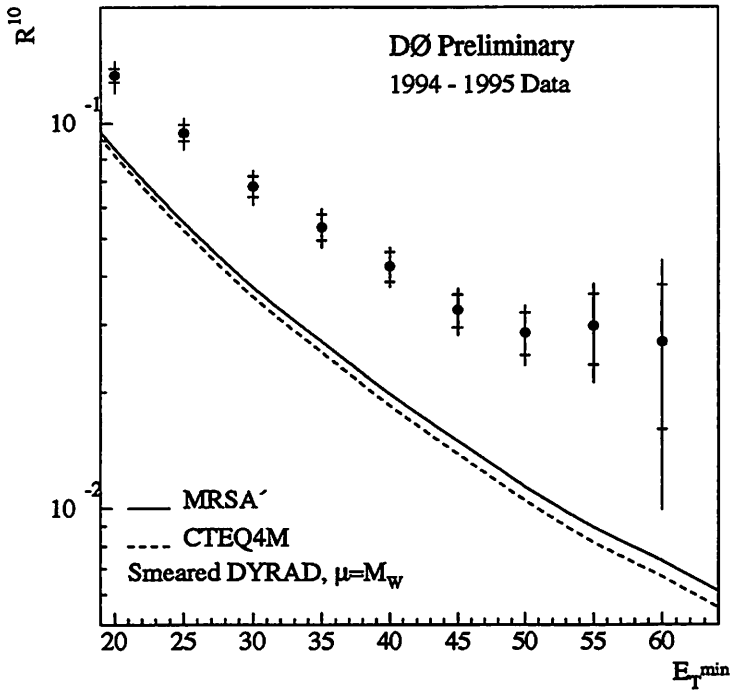

Figure 6.2: $\mathcal{R}^{10}$ versus E_T^{min} with CTEQ4M and MRSA'.

In Figure 6.1(a) calculations for the full CTEQ4 family are plotted as smooth curves. The same is done for the MRSA family in 6.1(b). Little dependence on $\alpha_s(M_W^2)$ is seen in the theoretical predictions.

Table 6.1 lists the values for the data point with statistical and systematic errors.

In order to compare the CTEQ4 and MRSA parton distribution functions Figure 6.2 has the curves for CTEQ4M and MRSA' plotted with the data.

Two interesting facts are quite plain. The measurement is higher than the theory for the entire range of E_T^{min}. The theoretical calculations of $\mathcal{R}^{10}$ do not have a large dependence on the value of α_s as can be seen by the lack of spread in the curves. This will be explored more in the next section.

6.3 $\mathcal{R}^{10}$ vs. α_S

The $\alpha_s(M_W^2)$ dependence can be studied in more detail by choosing one value of E_T^{min} and plotting the measurement as a horizontal band on an $\mathcal{R}$ vs.α_s plot. The theoretical calculations for different PDF's are plotted as points.

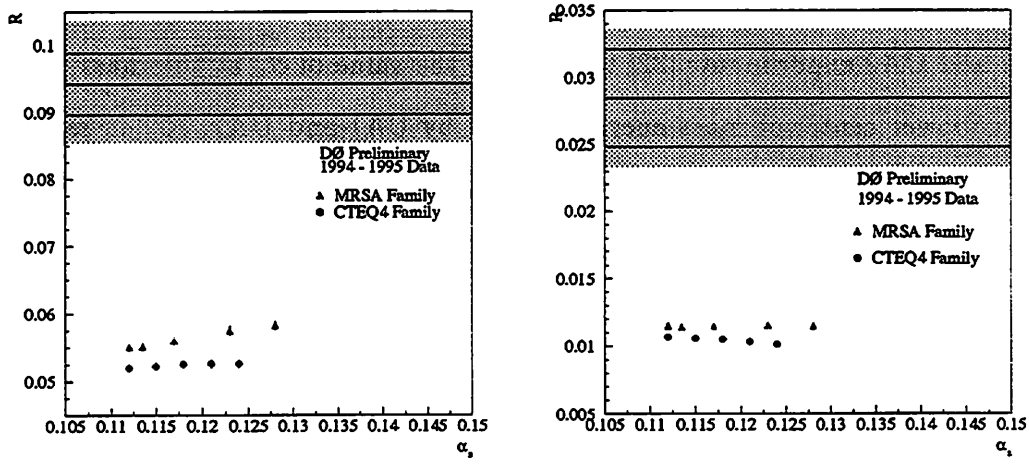

(a) E_T^{min}=25 GeV (b) E_T^{min}=50 GeV

Figure 6.3: $\mathcal{R}^{10}$ for E_T^{min} of 25 GeV and 50 GeV with DYRAD using CTEQ4 and MRSA parton distribution families.

Figures 6.3 plots the measured ratio for E_T^{min}= 25 GeV and for E_T^{min}= 50 GeV. The solid line is the measured value. The dotted lines are the statistical errors and the shaded band represents the statistical errors and all of the systematic errors added in quadrature.

The points in Figure 6.3 are the same NLO calculations made with DYRAD using the CTEQ4 family and the MRSA family of PDF's plotted at their respective values of $\alpha_s(M_W^2)$.

As can be seen in Figures 6.3 the theoretical calculations for varying values of

α_S exhibit little or no dependence on α_S.

This can be seen in more detail by studying $\mathcal{R}^{10}$ at a fixed value of E_T^{min}. The fact that the theoretical predictions for $\mathcal{R}^{10}$ versus α_S plot (Figure 6.3) display little to no dependence on $\alpha_S$indicates that something in the calculation is canceling the increase in the matrix elements as α_S is increased. A similar plot was used by the UA1 and UA2 experiments [32] to measure the value of α_S at the mass of the W. At the lower center of mass energy studied by UA1 and UA2, $\mathcal{R}^{10}$ is sensitive to α_S. As a check of the theoretical predictions I have verified that the calculations reproduce the UA2 results in this different kinematic regime.

6.4 Results

The ratio, $\mathcal{R}^{10}$, of the production cross sections for $W + 1$ Jet to $W + 0$ Jets has been measured as a function of the transverse energy cut, E_T^{min}, used to define a jet. The value of $\mathcal{R}^{10}$ for an E_T^{min} cut of 25 GeV is

$$\mathcal{R}^{10} = 0.0956 \pm 0.0046^{stat} \pm^{0.0081^{syst}}_{0.0077}. \tag{6.3}$$

For an E_T^{min} cut of 50 GeV the measurement is

$$\mathcal{R}^{10} = 0.0295 \pm 0.0036^{stat} \pm 0.0037^{syst}. \tag{6.4}$$

The corresponding theoretical predictions for CTEQ4M are

$$\mathcal{R}^{10}(25) = 0.0526 \pm 0.0006 \tag{6.5}$$

E_T^{min}	$\mathcal{R}^{10} \pm$ stat + high syst − low syst
20.0	$0.1343 \pm 0.0053 + 0.0127 - 0.0103$
25.0	$0.0956 \pm 0.0046 + 0.0081 - 0.0077$
30.0	$0.0693 \pm 0.0041 + 0.0059 - 0.0056$
35.0	$0.0548 \pm 0.0040 + 0.0048 - 0.0048$
40.0	$0.0434 \pm 0.0037 + 0.0035 - 0.0034$
45.0	$0.0336 \pm 0.0032 + 0.0034 - 0.0034$
50.0	$0.0295 \pm 0.0036 + 0.0037 - 0.0037$
55.0	$0.0311 \pm 0.0062 + 0.0060 - 0.0060$
60.0	$0.0286 \pm 0.0109 + 0.0131 - 0.0131$

Table 6.1: $\mathcal{R}^{10}$ as a function of E_T^{min} for CC electrons.

$$\mathcal{R}^{10}(50) = 0.0105 \pm 0.0002, \tag{6.6}$$

while the predictions using MRSA′ are

$$\mathcal{R}^{10}(25) = 0.0551 \pm 0.0006 \tag{6.7}$$

$$\mathcal{R}^{10}(50) = 0.0114 \pm 0.0002. \tag{6.8}$$

The rest of the results are in Table 6.1. The first error is the statistical error. The second and third errors are the high and low systematic errors respectively. The statistical error includes the statistical errors from the electron efficiency corrections (Table 5.1) and from the $\not\!\!E_T$ efficiency corrections (Table 5.4).

Studies of the dependence of the NLO calculation on different values of the renormalization and factorization scales were conducted by Giele *et al.* [7]. The conclusion was that the calculations display very little dependence on the scales.

Chapter 7

Conclusions

The measurement of $\mathcal{R}^{10}$ for an E_T^{min} of 25 GeV is over 4σ above the theoretical prediction and larger than the theory by a factor of 1.8 ± 0.2. The 50 GeV measurement is over 3σ above the theory and 2.6 ± 0.4 times larger.

The fact that the theory is lower than the data seems to imply that the theory is predicting too few $W + 1$ Jet events. The prediction from DYRAD for the total W cross section has been compared to the measurements made at DØ [33] and the two agree. This also points to the $W + 1$ Jet part of the ratio since the inclusive cross section is dominated by $W + 0$ Jets.

One possible explanation for the discrepancy between data and theory lies with the PDF's. The parton distribution functions are derived primarily from measurements of the structure function F_2 in deep inelastic scattering experiments at much lower energies. F_2 is most sensitive to the quark content of the proton.

Of the three main components of the proton, up quarks, down quarks and gluons, the gluon structure is the least well measured and therefore the least con-

strained in the PDF fits. A calculation by Berends et al. [34] predicted that approximately 50% of the $W + 1$ Jet events at the Tevatron would be from quark–gluon production. An underestimate of the gluon distribution at the relevant momentum fraction would affect the $W + 1$ Jet cross section much more than it would the $W + 0$ Jets cross section or the total cross section. However, it is not expected that the full discrepancy can be accounted for solely by the gluon distribution.

A preliminary result from the CDF experiment of $W+ \geq N$ Jets cross sections [35] displays a similar excess over theory for the $W+ \geq 1$ Jet cross section. The theoretical predictions used are leading order calculations combined with gluon showering and display a large dependence on the renormalization scale. For $Q^2 = M_W^2 + p_T^2$ the $W+ \geq 1$ Jet cross section is 1.7 times higher than the theory. This scale is similar to the $Q^2 = M_W^2$ scale used in the NLO DYRAD calculations. For a scale of $Q^2 = \langle p_T \rangle^2$, where $\langle p_T \rangle$ is the average p_T of all the partons in the event, the CDF result is consistent with their theoretical calculations.

The final interpretation of these measurements may have to wait. While part of the discrepancy may be due to poorly measured gluon distributions I do not believe the full discrepancy can be accommodated by the gluons. Since the quark distributions are well constrained an increase by a factor of 4 in the gluon distribution in the relevant momentum fraction regime would be necessary to bring the theory into agreement with the data. This still does not explain the lack of dependence on α_s for the NLO predictions at an E_T^{min} of 25 GeV or at an E_T^{min} of 50 GeV.

Bibliography

[1] Yu. Dokshitser, *Sov. Phys. JETP* **46**, 641 (1977),
V. N. Gribov and L. N. Lipatov, *Sov. J. Nucl. Phys.* **15**, 78 (1972),
G. Altarelli and G. Parisi, *Nucl. Phys.* B **126**, 298 (1977).

[2] D. Griffiths, *Introduction to Elementary Paricles*, (Wiley, New York, 1987).

[3] F. Halzen and A.D. Martin, *Quarks and Leptons: An Introductory Course in Particle Physics*, (Wiley, New York, 1984).

[4] V. D. Barger and D.J.N. Phillips, *Collider Physics*, (Addison–Wesley, New York, 1987).

[5] Peter B. Arnold and M. Hall Reno, *Nucl. Phys.* B **319**, 37 (1989)

[6] Howard Baer and Mary Hall Reno, *Phys. Rev.* D **43**, 2892 (1991)

[7] W.T. Geile, E.W.N. Glover and D.A. Kosower, *Nucl. Phys.* B **403**, 633 (1993).

[8] Joey Thompson, Fermilab Report FERMILAB-TM-1909, 1994 (unpublished).

[9] DØ Collaboration, S. Abachi *et al.*, *Nucl. Instrum. Methods* A **338**, 185–253 (1994).

[10] R. J. Genik II, Internal DØ Note, #2411, 1995 (unpublished).

[11] N. Amos, Internal DØ Note, #2072, 1994 (unpublished).

[12] M. Narain, in proceedings of the 7^{th} *Meeting of the American Physical Society Division of Particles and Fields*, edited by C. H. Albright, P. H. Kasper, R. Raja and J. Yoh (World Scientific, New Jersey, 1993), pp. 1678–1680.

[13] Jaehoon Yu, Ph. D. thesis, SUNY at Stony Brook, 1993 (unpublished), DØ Collaboration, S. Abachi *et al.*, *Phys. Rev. Lett.* **75**, 3226 (1995).

[14] T. Joffe-Minor, Internal DØ Note #3219, 1997 (unpublished)

[15] J. Yu, Internal DØ Note #1685, 1993 (unpublished)

[16] DØ Collaboration, S. Abachi *et al.*, *Phys. Rev.* D **52**, 4877 (1995).

[17] W. Carvalho and T. Taylor, Internal DØ Note #2798, 1995 (unpublished).

[18] J. Tarazi, Ph. D. thesis, University of California at Irvine, 1997 (in preparation).

[19] U. Heintz, Internal DØ Note #2268, 1994 (unpublished).

[20] I. Adam *et al.*, Internal DØ Note #2298, 1994 (unpublished).

[21] M. Demarteau, J. Sculli and K. Streets, Internal DØ Note #2929, 1996 (unpublished).

[22] Qiang Zhu, Ph. D. thesis, Columbia University, 1994 (unpublished).

[23] I. Adam *et al.*, Internal DØ note #2982, 1996 (unpublished).

[24] T. Joffe-Minor, Internal DØ Note #3218, 1997 (unpublished).

[25] R. Kehoe and R. Astur, Internal DØ Note #2908, 1996 (unpublished).

[26] M. Bhattacharjee *et al.*, Internal DØ Note #2887, 1996 (unpublished).

[27] B. Abbott *et al.*, Internal DØ Note #2885, 1996 (unpublished).

[28] J. Huth *et al.*, in proceedings of *Research Directions for the Decade, Snowmass 1990*, edited by E. L. Berger (World Scientific, Singapore, 1992).

[29] H. L. Lai *et al.*, *Phys. Rev.* D **55**, 1280–1296 (1997).

[30] A.D. Martin, R.G. Roberts and W.J. Stirling, *Phys. Lett.* B **356**, 89–94 (1995).

[31] R. Hirosky, Internal DØ Note #2369, 1994 (unpublished)
R. Hirosky, Internal DØ Note #2405, 1995 (unpublished)

[32] UA1 Collaboration, M. Lindgren *et al.*, *Phys. Rev.* D **45**, 3038 (1992), UA2 Collaboration, J. Alitti *et al.*, *Phys. Lett.* B **263**, 563 (1991).

[33] DØ Collaboration, S. Abachi *et al.*, *Phys. Rev. Lett.* **75**, 1456 (1995).

[34] F.A. Berends *et al.*, *Phys. Lett.* B **237**, 237 (1989).

[35] presented by J. Dittmann, at *32nd Rencontres de Moriond: QCD and High-Energy Hadronic Interactions*, Les Arc, France, March 22–29, 1997, (proceedings to be published).